



# Colloidal self-assembly concepts for light management in photovoltaics

**Matthias Karg<sup>2</sup>, Tobias A.F. König<sup>1</sup>, Markus Retsch<sup>2</sup>, Christian Stelling<sup>2</sup>, Paul M. Reichstein<sup>3</sup>, Tobias Honold<sup>2</sup>, Mukundan Thelakkat<sup>3</sup> and Andreas Fery<sup>1,\*</sup>**

<sup>1</sup> Physical Chemistry II, University of Bayreuth, Universitätsstr. 30, 95447 Bayreuth, Germany

<sup>2</sup> Physical Chemistry I, University of Bayreuth, Universitätsstr. 30, 95447 Bayreuth, Germany

<sup>3</sup> Applied Functional Polymers, Macromolecular Chemistry I, University of Bayreuth, Universitätsstr. 30, 95447 Bayreuth, Germany

Colloidal particles show interaction with electromagnetic radiation at optical frequencies. At the same time clever colloid design and functionalization concepts allow for versatile particle assembly providing monolayers of macroscopic dimensions. This has led to a significant interest in assembled colloidal structures for light harvesting in photovoltaic devices. In particular thin-film solar cells suffer from weak absorption of incoming photons. Consequently light management using assembled colloidal structures becomes vital for enhancing the efficiency of a given device. This review aims at giving an overview of recent developments in colloid synthesis, functionalization and assembly with a focus on light management structures in photovoltaics. We distinguish between optical effects related to the single particle properties as well as collective optical effects, which originate from the assembled structures. Colloidal templating approaches open yet another dimension for controlling the interaction with light. We focus in this respect on structured electrodes that have received much attention due to their dual functionality as light harvesting systems and conductive electrodes and highlight the impact of inter-particle spacing for templating.

## Introduction

The world's increasing energy demands along with gradually depleting fossil fuel stock and the detrimental effects of global warming require highly efficient energy conversion and storage from renewable energy sources. Photovoltaics (PV) is one of the main contenders in this field [1]. PV offers a broad diversity of systems ranging from the first generation opaque single crystal silicon solar cells up to third generation semitransparent organic and hybrid systems. The former absorb almost all the incident light energy within the band gap of the material and convert it efficiently into electrical energy under high light intensity conditions and therefore are mainly applied on roof tops or in solar energy parks. Here the main losses arise from reflection and thermal relaxation of hot electrons. In the latter, only a small fraction of incident light is absorbed and these systems work also

very well under diffuse light conditions making them suitable for indoor as well as building integrated applications [2]. Additionally, these lightweight thin film solar cells can be fabricated on flexible rolls using printing technologies and are suitable for lamination on curved surfaces or for automotive roof tops. However, it is a challenge to fabricate semitransparent solar cells maintaining high power conversion efficiency. This is due to the fact that the loss channels in thin film organic and hybrid systems are multifaceted; the transmission and reflection losses covering a major part of it. The thickness of the light harvesting and charge transporting layers in such systems are limited to <200 nm due to the restrictions of small exciton diffusion length and low charge carrier mobility. Thus, a main drawback of such devices is the comparably thin active layer that leads to rather weak absorption characteristics. Consequently the loss channels within the optical gap have to be minimized in order to improve the power conversion efficiency. Here light management using a combination of

\*Corresponding author: Fery, A. ([andreas.fery@uni-bayreuth.de](mailto:andreas.fery@uni-bayreuth.de))

different approaches is a necessity to improve the performance of the devices.

Much effort in recent years was devoted to the design and development of new active materials to improve the overall light harvesting [3] by extending the optical gap to the red region of the solar spectrum. Energy transfer within the absorbing layer via Förster resonance energy transfer (FRET) [4,5] and co-sensitization in dye-sensitized systems were also demonstrated [6,7]. In addition, independent of the device type, general light management approaches such as microcavity/optical spacer for wave guiding [8], use of scattering layers/structures [9] and plasmonics are also intensively investigated [10].

This review focuses on the use of colloidal particles in PV for an efficient light management. Specifically we address two aspects in detail, section 'Colloidal structures for light harvesting': the use of colloidal structures for light harvesting and section 'Template electrodes from colloidal assembly structures': their application as templates for the assembly of electrodes, which at the same time have light harvesting functionality. We aim to give an overview of concepts and rational materials design for using colloidal particles to enhance the performance of a fully functional PV device, that is, the colloids are not source of the charges generated. Thus, our discussion does not take into account effects such as direct electron extraction from, for example, metal nanoparticles such as gold and silver [11–14] as well as exciton formation and dissociation using semiconductor quantum dots [15–19].

The first section starts with an overview of the type of colloidal structures that have successfully been applied for light harvesting and categorizes them in terms of their use in specific PV systems and structure on the colloidal scale, thus setting the scene for the detailed discussion in the following sections. Colloidal particles have dimensions on the order or smaller than the wavelength of visible light and hence they possess size, shape and material dependent optical properties. Section 'Role of particles in PV' is dedicated to an in-depth discussion of these optical properties. In contrast to conventional lithographic approaches, which are usually used to create nano- and mesoscale light management structures, colloidal particles are typically prepared via wet-chemical synthesis. During the last century, a plethora of protocols for size- and shape-selective synthesis of colloidal particles from different materials has been developed [10], [20–23]. In section 'Particle design: size, shape, material', we will review the synthesis of well-defined colloidal particles with special attention to the requirements for light harvesting applications. Section 'Particle functionalization' deals with the functionalization of colloidal particles that allows for the controlling of (i) inter-particle interactions, (ii) inter-particle spacing from nanometers up to microns, (iii) complex colloidal surface assemblies and (iv) surface coverage. In section 'Local and collective coupling effects', the impact of assembly on optical properties and the appearance of novel optical features such as local inter-particle coupling effects and collective long range resonances will be discussed in detail. Part 2 is dedicated to ordered nano- and mesostructures obtained via colloidal templating. Here the colloidal particles themselves do not act as functional features, but rather colloidal assemblies are used as sacrificial masks for lithographic processes. This opens a new parameter space, where the functionality of the PV device can be custom designed starting with the supporting substrate or

electrode interface. Colloidal lithography can be combined with sol-gel, evaporation, and reactive-ion etching techniques, which in many cases will not only add highly ordered nanostructures to a PV system, but also often results in a defined topography with increased surface area. Section 'Structured electrodes from close-packed colloidal monolayers' illustrates the formation of structured electrodes from close-packed colloidal monolayers. Here predominantly individually separated nanostructures are accessible. In section 'Structured electrodes from non-close-packed colloidal monolayers', non-close-packed colloidal monolayers will be discussed, which can be used to obtain percolated structures, which for instance allow the excitation of propagating surface plasmons, or may be used as future transparent conducting electrode materials.

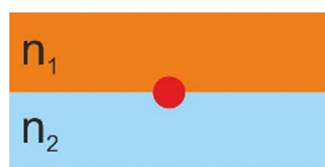
### Colloidal structures for light harvesting

The implementation of colloids in PV devices represents a promising route for light management tasks in particular for thin-film solar cells [10,20,21,24–28]. The optical effects, which are achievable by colloids are manifold and they can be grouped into the following two types depending on the parameters defined by the nature of the building blocks and the assembly structure.

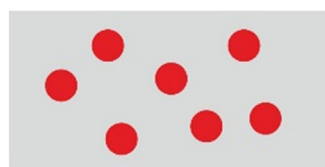
- (1) Parameters adjustable through the colloid design: Composition, size, shape, size- and shape-distribution, stability, functionalization, particle spacing.
- (2) Parameters adjustable through the assembly process: Colloid distribution, surface coverage, inter-particle distance, periodicity.

Furthermore the location of the particles within the device is crucial for the optical performance and needs to be chosen depending on the desired effect [29]. Figure 1(a) illustrates schematically the resulting refractive index conditions for particles being embedded either in the active medium ( $n_1 = n_2$ ) or for particles located at an interface such as the interface between the electrode and the active matrix ( $n_1 \neq n_2$ ). For the sake of clarity the sketch is over simplified: More than two layers with different refractive indices might actually influence optical properties of the colloid. Furthermore the surrounding materials may be different in chemical composition but exhibit a nearly equal refractive index ( $n_1 \sim n_2$ ) or provide an effective average refractive index environment. In addition the position of the colloid at or near the interface may differ from a contact angle of  $90^\circ$  as shown in Figure 1(a). Table 1 gives an overview of exemplary studies where the different refractive index conditions are utilized in devices for the scenarios of  $n_1 = n_2$ ,  $n_1 \approx n_2$ , and interface  $n_1 \neq n_2$ .

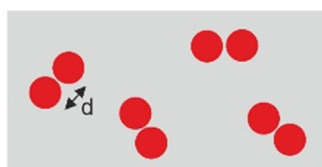
Another important factor, which determines the optical behavior of colloids in PV devices is the particle distribution. Figure 1(b) shows schematically random distributions of single or clustered particles. In a random arrangement of single particles an average nearest distance can be determined. If these distances  $l$  is much larger than the particle diameter the optical properties of the layer will resemble the properties of the single building blocks. Thus, no cooperative effects are found. This situation is different for randomly distributed clusters consisting of two or more particles with a center-to-center distance  $d$ . At small values of  $d$  the clusters will significantly differ in their optical response compared to single particles. The detailed effects of particles in close proximity will be discussed in section 'Local and collective coupling effects'.

(a)  
Particle location

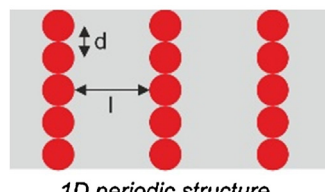
$n_1 = n_2$ : particle in matrix  
(e.g. active medium)  
 $n_1 \neq n_2$ : particle at interface  
(e.g. electrode, glass)

(b)  
Random particle structures

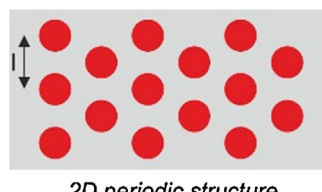
Single particle



Clustered particles

(c)  
Ordered particle structures

1D periodic structure



2D periodic structure

**FIGURE 1**

Schematic depiction of the particle location (single particle) in a PV device (a) reduced to the refractive index environment in the particle vicinity. If  $n_1 = n_2$  the particle is embedded in a homogeneous refractive index matrix, which can be the active matrix of a PV device. For different refractive indices  $n_1 \neq n_2$  the particle is located in or near an interface of two materials. This could be for example the solid support (glass) or the electrode. Examples for experimental PV studies where colloids are embedded in such index matrices are listed in Table 1 (b,c) show different scenarios for particle distribution within a PV device. Random particle structures can either consist of individual colloids with fairly large inter-particle distances or clustered particles such as dimers and trimers, which show small inter-particle separations within the clusters but no order of the clusters themselves. Ordered particle structures can have 1D or 2D periodicity when introduced as a monolayer. The length scales are depicted as center-to-center distance  $d$  and periodicity  $l$ .

Besides random arrangements of particles as an optically functional layer, introducing order can lead to additional effects. Figure 1(c) shows examples for 1D periodic structures (particle lines) and non-close-packed hexagonal 2D monolayers. In the 1D example two length scales become important because the particle pattern has no rotational symmetry: The center-to-center distance  $d$  of particles within the particle chain and the periodicity  $l$ , which is the line-to-line separation in this example. For  $l = d$  a square structure results. The 2D hexagonal monolayer shows rotational symmetry and is consequently characterized by one length scale  $l$ , which is the lattice constant. If  $l$  equals the particle diameter, neighboring particles are in contact and a close-packed monolayer is obtained. The given examples shall illustrate the variety of structures and relevant length scales.

Theoretical studies can help to decide for the most promising design rules. Qu et al. investigated the influence of the particle

position on the solar cell performance [46]. The most efficient location turned out to be the interface between a poly-3,4-ethylenedioxithiophene:polystyrene sulfonate (PEDOT:PSS) charge injection layer and the photoactive layer consisting of poly(3-hexylthiophene):(6,6)-phenyl-C61-butyric-acid-methyl ester (P3HT:PCBM). Furthermore, they evaluated a range of particle sizes and spacing  $l$ , which can additionally increase the absorption. Particle diameter of 10–28 nm were found to improve the device efficiency effectively. The optimum ratio of particle diameter to particle spacing was in the range of 1.1–3.8 for particles at the PEDOT:PSS/P3HT:PCBM interface. Similarly, Zhu et al. showed in their modeling that particle size and particle spacing of metal nanospheres incorporated as hexagonal periodic arrays are important parameters for the performance of organic PV devices [47]. The authors determined the light concentration factor for 5, 10, 15 and 20 nm silver spheres in P3HT:PCBM and PCPDTBT:PCBM devices. The maximum light concentration factor depends on the photoactive layer. However, for center-to-center distances much larger than the particle size the concentration factor reduces to 1. They also deduced from their model that even a very thin spacer/insulator layer (<5 nm) on top of an Ag nanoparticle strongly reduces the degree of light concentration.

*Role of particles in PV*

The photon-exciton conversion rate and the exciton diffusion to an interface to dissociate and charge collection are the main limiting factors for the maximum efficiency of PV devices. In particular thin-film semitransparent solar cells suffer from weak absorption of light [10,21,22,48]. Here light management becomes essential to influence the photon-exciton conversion. The absorption becomes optimal when the reflection and transmission are minimal. Scattering into and inside the active layer can enhance the overall absorption, whereas diffuse reflection at the device interfaces should be suppressed. This has to be realized over the whole solar spectrum, independent from the polarization and angle of incidence [49].

Figure 2(a) shows the solar spectrum of air mass (AM) 1.5 [50] and its integration, which is proportional to the maximum attainable photocurrent. In addition the band gaps or optical gaps of different materials, frequently used in PV, are highlighted as dashed lines (n-type Si [51], P3HT [52], and poly[2,6-(4,4-bis(2-ethylhexyl)-4H-cyclopenta [2,1-b;3,4-b']dithiophene)-alt-4,7(2,1,3-benzothiadiazole)] (PCPDTBT) [53]). The spectrum defines our region of interest for light management structures. Colloids have typically dimensions below or in the range of the wavelength of visible light and can significantly interact with the electromagnetic radiation by both scattering and absorption [54]. We will first focus on scattering, as it is the most generic effect and dominant for most dielectric particles used in PV light harvesting. For particles with diameters  $D \ll \lambda/20$  the scattering intensity is isotropic and follows a  $\lambda^{-4}$ -dependence (Rayleigh scattering). Hence the scattering intensity of Rayleigh scatterer increases with decreasing wavelength  $\lambda$  (see calculation for  $\text{SiO}_2$  in Fig. 2(b)). This is desired for PV applications as it matches the solar spectrum in the IR and visible region. For larger particles the distribution of scattering centers within one scattering object become important and a complex angular-dependence is found due to interference effects (Mie scattering [55]). In general increasing particle size of colloids leads to an increase of the integrated scattering intensity.

TABLE 1

**Overview of exemplary studies using colloids embedded in different refractive index (RI) environments as schematically illustrated in Fig. 1(a). The conditions ( $n_1 = n_2$ ) and ( $n_1 \approx n_2$ ) stand for particles embedded into the photoactive matrix, whereas ( $n_1 \neq n_2$ ) represents that the particles are at the interface.**

RI environment	Reference	Particle location	Device
$n_1 = n_2$	Baek et al. [30]	Ag nanoparticle in PEDOT:PSS layer	Organic
	Fu et al. [31]	Au nanoparticle in PEDOT:PSS layer or in hybrid PCPDTB:CdSe layer	Organic and hybrid
	Gangishetty et al. [32]	Au@SiO <sub>2</sub> nanoparticle in TiO <sub>2</sub> -matrix	Dye-sensitized
	Lu et al. [33]	Au and Ag nanoparticle in PEDOT:PSS layer	Organic
	Paci et al. [34]	Ag nanoparticle in P3HT:PCBM layer	Organic
	Qi et al. [35]	Ag and Ag@TiO <sub>2</sub> nanoparticles in TiO <sub>2</sub> photoanode	Dye-sensitized
	Spyropoulos et al. [36]	Au nanoparticle in P3HT:PCBM layer	Organic
	Yang et al. [28]	Au nanoparticle in PEDOT layer	Tandem
	Wang et al. [27]	Au nanoparticle in P3HT:PC <sub>70</sub> BM layer	Organic
	Sheehan et al. [37]	Au@SiO <sub>2</sub> and Au@SiO <sub>2</sub> @TiO <sub>2</sub> nanoparticle in photoactive matrix	Dye-sensitized
$n_1 \approx n_2$	Standridge et al. [38]	Ag nanoparticle in photoactive matrix	Dye-sensitized
	Wooh et al. [39]	Au@SiO <sub>2</sub> nanoparticle in photoactive matrix	Dye-sensitized
	Xu et al. [40]	Al nanoparticle in photoactive matrix	Dye-sensitized
$n_1 \neq n_2$	Grandidier et al. [41]	SiO <sub>2</sub> particle on front (ITO/air interface)	a-Si:H
	Pastorelli et al. [42]	Au nanoparticle at interface ITO/TiO <sub>2</sub> layer	Organic
	Choi et al. [29]	Au@SiO <sub>2</sub> at interface ITO/PEDOT:PSS and at interface PTB7:PC <sub>70</sub> BM/PEDOT:PSS	Organic
	Brown et al. [43]	Au@SiO <sub>2</sub> at interface TiO <sub>2</sub> /hole-transport layer	Dye-sensitized
	Kawasaki et al. [44]	Au nanoparticle at ITO/TiO <sub>2</sub> interface	Dye-sensitized
	Yoon et al. [45]	Ag nanoparticle at interface PEDOT:PSS/photoactive layer	Organic

A possible route to enhance the photoinduced charge generation rate in a PV device is to enhance the path length of the incident photons within the device. This can be realized by implementing sub-wavelength scattering centers at the front and/or the rear of the cell. Here, colloidal particles are very promising since the scattering performance can be tailored over a broad range by materials selection, particle size and geometry. Another important parameter is the refractive index of the scattering object in relation to the embedding matrix. In case of index matching between these two phases, no scattering will occur at all.

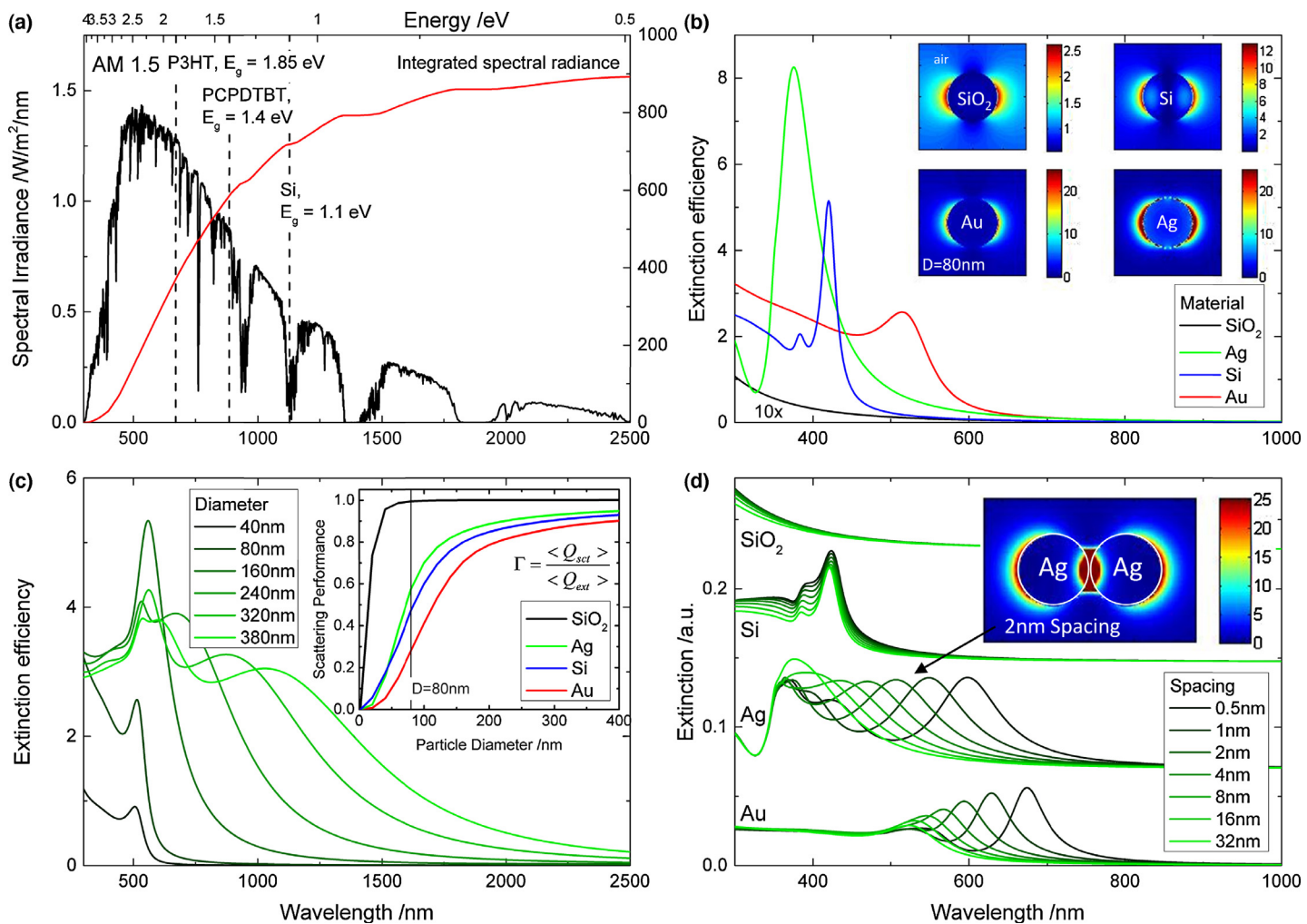
Whereas particles from dielectric materials interact with electromagnetic radiation predominantly via scattering, the situation is more complex for metal colloids due to their complex dielectric function. Figure 2(b) shows the extinction efficiencies of spheres of different materials (Silica, Au, Ag, Si) with 80 nm in diameter. The spectral overlap with the solar spectrum is visible although the origin of the extinction is different: For silica the extinction is simply caused by scattering as previously discussed. For Si, Ag and Au the extinction is not only influenced by scattering but also absorption, which leads to distinct peaks. The most frequently studied examples for colloids with absorption properties in the relevant wavelength range for PV applications are particles of the noble metals silver and gold [56]. When reduced to the nanosize, such metal colloids show strong absorption peaks due to collective oscillations of the electrons of the conduction band. These so-called localized surface plasmon resonances (LSPR) are determined by a single peak for rather small particle sizes, which resembles the dipolar mode. In Fig. 2(c) simulated extinction profiles for gold nanoparticles of different diameter from 40 to 380 nm are shown.

These calculations were realized by the authors using Mie theory [57] for monomers, generalized multiparticle Mie theory (GMMT) [58] for dimers, and finite-difference time-domain (FDTD) [59] modeling for the intensity plots. The plasmon resonance at largest wavelength is always related to a dipolar mode. Additional higher modes (quadrupolar, octupolar) are excited for larger particle sizes [60]. It is also characteristic that the scattering cross-section increases with increasing size. This is demonstrated by the calculated scattering performance shown in the inset in Fig. 2(c) [26]. A balance between scattering and absorbance cross-section is achieved at 80 nm. Thus the absorptive loss plays a crucial role if plasmonic particles are of interest as scattering objects in PV [25]. Particle size has also a pronounced effect on the wavelength position of the absorption band. The position of the LSPR  $\lambda_{LSPR}$  as a function of particle size can be quantified by the following scaling law (allometric power law) [61]:

$$\lambda_{LSPR}(D) = kD^a + c \quad (1)$$

In this equation,  $k$  is an amplitude parameter,  $D$  the sphere diameter (apply without unit),  $a$  the scaling exponent and  $c$  is an offset parameter. The values for  $k$ ,  $a$  and  $c$  will directly depend on the surrounding refractive index. For water (air) as surrounding material the parameters are as followed:  $k = 0.0005$  nm (0.0001 nm),  $a = 2.52$  (2.63), and  $c = 525.1$  nm (505.4 nm). In general an increase in refractive index will cause a plasmonic resonance redshift along with an increase in cross-section intensity [61].

Due to their plasmon resonance, metal nanoparticles exhibit strong, localized electric fields [62]. These near-fields are of great interest for enhancing the photon-exciton conversion in PV

**FIGURE 2**

Simulated extinction for different colloidal systems for absorption and scattering enhancement. (a) Solar spectrum and integrated spectral radiance which is proportional to the photocurrent. (b) Extinction efficiency and enhancement factor of a dielectric (silica), a metalloid (or semiconductor c-Si) (silicon), and metallic nanoparticles (gold and silver) of 80 nm diameter. (c) Extinction efficiency of gold nanospheres in air with different particle diameter and scattering performance (shown in inset for different nanoparticles). (d) Extinction cross-section of a nanoparticle dimer at various inter-particle distances (spacing). Electric field intensity plots imaged at resonance frequency (units  $|E|^2/|E_0|^2$ ).

devices [63,64]. Hence it is often desired to control the strength and range of these fields. The magnitude and the number of the near-field resonances is strongly dependent on the type of metal, the size and shape of the particle as well as the inter-particle distance: For increasing particle size the strength of the near-field and its spatial dimensions rise. The number of resonances is inversely proportional to the symmetry axes of the particle. For instance, nanospheres only show one resonance, whereas nanocubes have lower symmetry axis and show up to six resonances [65,66]. Figure 2(b) shows the extinction efficiencies of spheres of different materials (Silica, Au, Ag, Si) with 80 nm in diameter. While for the silica sphere only local field intensities up to 2.5 are calculated, the values for gold and silver spheres are approximately ten times higher. Furthermore this enhancement can be significantly increased when particles are brought into close vicinity to each other. As can be seen from the results of FDTD simulations for a pair of silver spheres shown in the inset graphic in Fig. 2(d), the electric field is the highest in the particle gap. The optical interaction between approaching colloids will be treated in detail in section ‘Local and collective coupling effects’.

The question of how the incorporation of plasmonic particles is actually enhancing the performance of thin film solar cells is still under debate. It critically depends on the design of the PV device and the observed enhancement has been attributed to light scattering at the particles [27], or contributions from (plasmonic) near-field enhancement [30] or both. Furthermore, metallic particles on top of a Si solar cell can act as antireflective coatings [67]. Wang et al. investigated the difference between a 10 nm and 70 nm gold nanoparticle, which were incorporated into the photoactive layer. The Au colloids not only increased the light absorption via light scattering, but also improved the charge transport through the active layer. Remarkably, metallic particle surfaces have not been passivated, which is usually done to prevent exciton quenching and unwanted recombination [35]. Baek et al. immobilized a range of differently sized Ag nanoparticles in the hole conducting layer at high volume fractions (40%) [30]. They found a clear correlation between the Ag nanoparticle size, its plasmonic resonance and the maximum external quantum efficiency (EQE) of the device. For a PCPDTBT/PCBM based solar cell Ag nanoparticle of 67 nm in diameter featured the highest enhancement of 13% at a power

conversion efficiency (PCE) of 7.6%. For this nanoparticle size the authors have also investigated the influence of particle concentration on the device performance. A concentration of  $4.5 \times 10^9$  particles/cm<sup>2</sup> was found to yield an optimum in PCE and short circuit current density ( $J_{sc}$ ). For higher concentrations, decreasing  $J_{sc}$  and fill factor (FF) values were observed. This reduced performance was related to the formation of particle clusters during the deposition of higher amounts of particles. This example nicely illustrates that not only particle size is an important parameter for colloidal light management in PV, but also the particle concentration and particle separation are crucial.

An interesting alternative to influence the absorption and scattering of plasmonic nanoparticles over a broad range of wavelength is given by the preparation of hollow metal nanoshells. The optical properties of such nanoshells are directly determined by the nanoshell dimensions. These hollow metal structures have very high extinction cross-sections but still show sufficient colloidal stability compared to metal spheres of similar size. The absorption and scattering behavior of the nanoshells can be precisely tuned by variation of their outer and inner diameter [68,69]. Recently Paz-Soldan et al. have employed gold nanoshells with finely tuned spectral properties (scattering-to-absorption ratio) to enhance the performance of quantum dot solar cells in a specific spectral range where the cell performance is rather low [70]. The authors have combined experimental and theoretical descriptions to find the ideal match in spectral properties of the plasmonic and the excitonic material. As compared to non-plasmonic reference cells a PCE enhancement of 11% was found. In the near-infrared a peak enhancement of 35% was measured. This example shows that rational design of colloidal particles with well-defined optical properties is a promising way to enhance the performance of PV devices.

From the examples and considerations provided in this section it becomes apparent that colloidal building blocks inherently possess a huge potential to influence light management in PV devices. The main factors are scattering, absorption, and local field enhancement, which intricately depend on the type of the particle as well as its surrounding medium. Their effect on the electrical performance as well as reflection and transmission at the interfaces may also not be neglected, though. Since particle composition, size and shape are of utmost importance, the following section will focus on synthetic approaches for controlling these parameters.

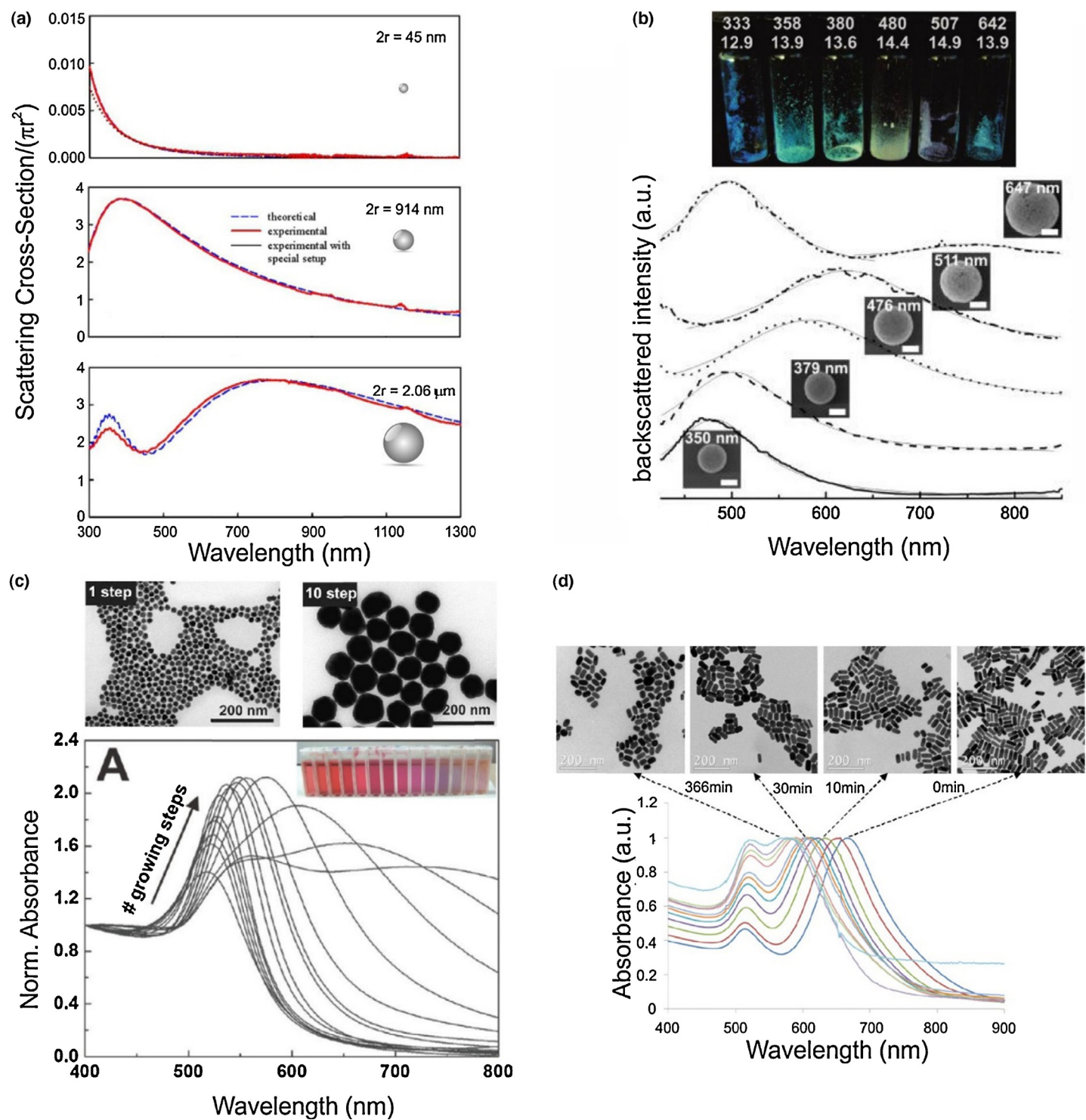
#### *Particle design: size, shape, material*

Nowadays a plethora of colloids with tailored optical properties is available since the number of works dealing with the synthesis of colloidal systems with controlled composition, particle size and particle shape has steadily increased during the last decades. Choosing the 'right' particles for PV applications is complex because the ideal composition, size and shape will depend on the desired type of enhancement effect (e.g. scattering or near-field enhancement) as well as the device layout, amongst other parameters such as chemical and electrical compatibility. Up to now most of the examples in the literature where colloids have been employed as light management structures in PV applications focus on particles which are nearly monodisperse in size and shape. Hence the particles used have well-defined scattering, absorption

and near-field properties. Thus optical properties can be precisely tailored to match for example the extinction of the active layer. In addition, theoretical simulations are much easier to be performed for a monodisperse system. However, depending on the enhancement effect and the type and layout of the device, colloids with polydispersity in size and shape, and even in composition may also be well suited for application in PV, although a quantitative correlation with device performance has not been realized. Nevertheless there are many examples in the literature which clearly require monodisperse colloids as for example when these are used as photonic bandgap elements. In particular, colloidal polymer particles such as polystyrene or polymethyl methacrylate are of relevance because they are rather cheap and easily available through emulsion polymerization [71,72]. This method can provide colloidally stable polymer particles with sizes which can be controlled by the amount of surfactant employed in the polymerization. Other common approaches for the preparation of such particles are miniemulsion [73,74] and emulsifier-free [75,76] polymerizations. Figure 3(a) shows measured and fitted scattering cross-sections of polystyrene particles of various sizes. For small sizes the scattering data can be well-described as Rayleigh scattering. For larger particle sizes Mie scattering is observed. The scattering cross-section increases significantly with increasing particle size. In addition the spectral range where effective scattering is observed changes with increasing diameter. Thus, polymer particles with dimensions, comparable to the wavelength of visible light are promising candidates as scattering centers and as building blocks for photonic structures in PV. Apart from polymer based materials, silica particles have been shown to be suitable for efficiency enhancement in PV devices [77,78]. Monodisperse silica colloids can be prepared by the well-known protocol of Stöber et al. [79]. This method relies on hydrolysis and subsequent condensation of a silica precursor in alcohols under basic conditions providing particles with diameters ranging from 50 nm to 2000 nm can be achieved. Cheaper approaches are available if monodispersity is less important [80].

While a clear advantage of silica- and polymer-based materials is the low cost and easy preparation, the rather low scattering cross-section (compare Fig. 2(b)) limits their use in PV applications. The scattering performance can be significantly altered if hollow silica spheres are prepared. Figure 3(b) shows photographs and back-scattering spectra of hollow silica particles with different overall diameter but rather constant shell thicknesses [81]. Mie scattering in the visible wavelength range is observed. The effective refractive index of such hollow structures is determined by the particle diameter, shell thickness, and the shell material. Expectedly, the scattering cross section drops with decreasing aspect ratio between shell thickness and particle radius. However, the transport mean free path of light increases considerably at the same time in such dry particle powders. Interestingly, when embedding hollow spheres into a matrix material, the hollow core with its low refractive index ( $n = 1.0$ ) can then act as strong scattering center, due to the high contrast to the surrounding medium, which for most polymers is around  $n = 1.5$  [61].

Probably the most frequently applied colloidal systems in PV devices are gold and silver nanoparticles. A simple route to prepare gold nanoparticles of about 20 nm in diameter is the well-known citrate reduction protocol by Turkevich et al. [82]. This method

**FIGURE 3**

Tunable light manipulation with non-absorbing (a,b) and absorbing (c,d) colloids. (a) Size dependent Rayleigh (1) and Mie (2,3) scattering of polystyrene spheres [108]. The scattering cross section increases with increasing particle size, whereby the largest spheres show typical Mie type II scattering oscillations at shorter wavelengths. (b) Single particle spectra of hollow silica nanoparticles obtained by confocal dark field spectroscopy [81]. The insets show SEM images of hollow silica spheres and the visible Mie scattering of vials with different hollow nanoparticles. The scale bars correspond to 200 nm and the numbers on top of the vials indicate the overall particle diameter and shell thickness in nm, respectively. (c) Size controlled absorbance of spherical gold nanoparticles [90]. Increasing the particle size results in a red shift of the localized surface plasmon resonance. Two representative TEM images of the highly monodisperse spherical particles are shown. (d) Gold nanorods with finely tuned plasmon resonances prepared via thermal reshaping [103]. Shown are UV-Vis absorbance spectra and respective TEM images after different times of thermal treatment. © (a) AIP Publishing LLC, (b-d) American Chemical Society.

yields nearly spherical, polycrystalline particles, which show a dipolar LSPR at around 520 nm. Frens et al. have studied the effect of the concentration of the reducing agent citrate systematically and showed that particles ranging from 12 to 150 nm in diameter can be prepared [83]. Similarly Kimling et al. have examined the reaction conditions using citrate and ascorbic acid and found that narrowly distributed particles with sizes ranging from 9 to 120 nm are accessible [84]. While these protocols yield gold particles of low polydispersity with sizes relevant for PV applications, the volume fraction is low in all of these methods. Li et al. have recently shown that the achievable concentration can be significantly increased (about 5 times higher) using sodium hydroxide and controlled reaction temperatures [85].

Smaller gold particles can be prepared using stronger reducing agents but are of less relevance for PV applications due to their weak scattering/absorption. In contrast, larger particle sizes are often required. A well-established route toward larger particle sizes is based on seed-mediated growth. The advantages of this procedure are monodisperse particles and the possibility to fine tune particle size by the ratio seeds/metal precursor [86–88]. A disadvantage of these seed-mediated methods is the typically large amount of surfactant used during the growth of particles. Thus, excessive cleaning is required, which increases the cost of the material. Niu et al. have shown a one-step seed-mediated synthesis, without using large amounts of surfactants for stabilization, based on gold nanoparticle seeds prepared by the method of Frens [89]. The authors have used 2-mercaptosuccinic acid as reducing agent in the seeded growth of particles up to sizes of 150 nm. Solely using citrate Bastus et al. reported recently on a modified citrate reduction route, which allows for generation of particles of different diameter [90]. Figure 3(c) shows two representative TEM images of nearly spherical gold nanoparticles along with UV-vis absorbance spectra of a series of gold nanoparticles with increasing diameter prepared by this method. A clear red-shift of the LSPR with increasing particle diameter is observed. For larger particle sizes, additional plasmon modes appear and the absorbance is large over a broad range of wavelength. However, the plasmon resonance of gold is strongly damped which leads to rather high absorptive losses and a limited near-field enhancement [91]. When considering the near-field enhancement, silver nanoparticles are more promising compared to gold nanoparticles because their LSPR is less damped. For PV applications silver is also a much more interesting material due to its significantly lower price compared to gold but bares the risk of oxidation. Very similar to the Frens method for preparing gold nanoparticles, Li et al. have synthesized nearly monodisperse, spherical silver nanoparticles using citrate and ascorbic acid in the presence of iodide ions [92]. This way the authors could prepare silver nanoparticles with sizes of 20–40 nm stabilized by citrate. More recently Li et al. have reported on the size controlled synthesis of silver nanoparticles from different silver precursors [93]. The particle size could be controlled in a diameter range of 16–30 nm. The dipolar LSPR of these particles are located around 400 nm. Extending the diameter range Evanoff et al. have prepared silver nanoparticles of nearly spherical shape in the size range of 15–200 nm by the reduction of silver(I) oxide by hydrogen gas [94]. The same authors have also studied the extinction, scattering and absorption cross-section of these particles in detail [95]. The

smaller particles showed only dipolar LSPR modes at wavelength around 400 nm. Exceeding a particle diameter of around 90 nm, a quadrupolar contribution appeared close to 420 nm whereas the dipolar mode shifted toward higher wavelength for increasing particle size. Bastus et al. have reported on the size selective synthesis of silver nanoparticles with diameter ranging from 10 to 200 nm stabilized by citrate [96].

The near-field and far-field optical properties of gold and silver nanoparticles can be significantly manipulated by introducing non-spherical symmetry. During the last decade many protocols have been published allowing for the synthesis of noble metal nanoparticles with non-spherical shapes. Shape control of noble metal colloids is achievable through seed mediated growth. This two-step strategy allows for the synthesis of well-defined colloids through the separation of nanocrystal nucleation and selective growth of individual facets. At first, uniform seed particles are synthesized through reduction of metal ions in the presence of a suitable strong reducing agent. In the second step metal ions and shape templating molecules or surfactants are added which can result in non-spherical overgrowth. This way for example particles with rod-shape [97], triangular shape [98], nanodecahedra [99], nanostars [100], and nanocrystals with defined platonic shapes [101] can be synthesized. Particularly interesting are rod-shaped plasmonic nanoparticles due to their well-pronounced resonances, which are polarization dependent [102]. Collective oscillations of the valence electrons along the long axis of such rods cause a very intense longitudinal plasmon resonance. The position of this resonance can be finely tuned over a broad range of wavelength by adjusting the aspect ratio of the rods. This can be achieved for example either by the growing conditions [97] or by thermal decomposition [103]. Figure 3(d) shows absorbance spectra for gold nanorods of different aspect ratios obtained after different times of thermal treatment. They show two distinct absorption features: The transversal mode at around 520 nm and the longitudinal mode at longer wavelength. Reducing the aspect ratio of the nanorods leads to a pronounced blue shift of the longitudinal resonance whereas the transversal mode remains nearly unaffected. Hence tuning the aspect ratio of rods is a powerful means to control the absorbance properties. For more detailed information on size and shape selective synthesis of noble metal nanoparticles the reader is referred to the following reviews [54,104–107]. The concept of broadband plasmonic resonance tuning has been nicely demonstrated by Lu et al. [33]. They embedded 40 nm – 50 nm Au or Ag nanoparticles in the PEDOT:PSS layer and achieved the highest PCE of 8.67% for a blend of both particle types, which featured plasmonic resonances at 425 nm and 529 nm, respectively. They expanded this concept further by the use of Au rods of 40 nm – 50 nm in length and 15 nm in width, which translated into plasmonic resonances at 515 nm (transversal) and 679 nm (longitudinal). The absorption enhancement in the EQE spectra resulted in a high PCE of 8.41% - comparably high to the Ag/Au blend.

These examples of colloidal design extent their multiple influences on light management in PV devices as outlined in section 'Role of particles in PV', where scattering, absorption and local field enhancement were key, to multicolor photon management.

While the previous section has presented design routes toward synthesis of particles with well-defined optical properties, the integration of these particles typically requires additional surface functionalization, in order to ensure colloidal stability as well as compatibility with the matrix material and controlled particle distribution/surface coverage. Thus the following section will introduce concepts for surface functionalization of particles.

### Particle functionalization

Colloidal particles are typically metastable since in thermodynamic equilibrium aggregation of particles due to van der Waals interaction is favorable. This aggregation leads to a significant change or even loss of the single particle properties such as the well-defined localized surface plasmon resonances. Furthermore, the stability of colloids plays a major role for particle assembly, where uncontrolled aggregation usually needs to be prevented. Thus, the colloidal stability is a crucial aspect for the preparation of colloidal light harvesting structures with well-defined optical properties. Stabilization requires repulsive interactions. These can be electrostatic interactions, which strongly depend on the ionic strength, and/or steric stabilization. Increasing ionic strength can be used to lower the repulsive electrostatic interactions. This way the particle-particle separation upon particle assembly can be reduced. It has been shown that the addition of salt can be used to obtain monolayers of gold and silver nanoparticles with controlled inter-particle distances in solar cell devices [12]. In this work a balance between high surface coverage and well-defined separation between individual particles was achieved enabling plasmonic layer with characteristic extinction properties.

Apart from electrostatic repulsion, stability in many colloidal systems relies on steric effects. Steric stabilization typically relies on a corona of chains attached to a nanoparticle surface. These chains prevent direct contact between the surfaces of neighboring nanoparticles. Increasing the chain length of the stabilizer moieties can be employed to enhance stability and to increase the average particle-particle separation. To a certain extent this can be used to tune particle-particle separations in ordered particle arrays.

Many wet-chemical synthesis protocols provide particles which are already stabilized either by charged functionalities (e.g. carboxyl-, sulfate-, sulfonate-, amine- and amidine-groups), by rather bulky and flexible moieties providing steric stabilization or by a combination of both (electrosteric stabilization), because colloidal stability during synthesis is crucial. This functionalization however is in most cases not at all optimized for the structural requirements of subsequent assembly or for integration into PV systems. Thus changing the particle surface by ligand exchange or by growing a shell around the colloids is required. Ligand exchange allows tailoring the polarity of the particles, which can be used to perform phase transfer from one solvent to another or optimize them in their compatibility with the PV matrix [111,112,126–128]. Both shell growth and ligand exchange allow controlling inter-particle distances with respect to PV applications. Dielectric shells are ideally suited since they do not significantly alter the optical properties of the encapsulated colloid. Such shells ideally coat the colloids homogeneously and possess a defined thickness. When two of these core-shell colloids are brought into contact the shell can act as a spacer and the spacing  $d_s$  of the colloidal cores will be twice the shell thickness in case of non-deformable shells. A good

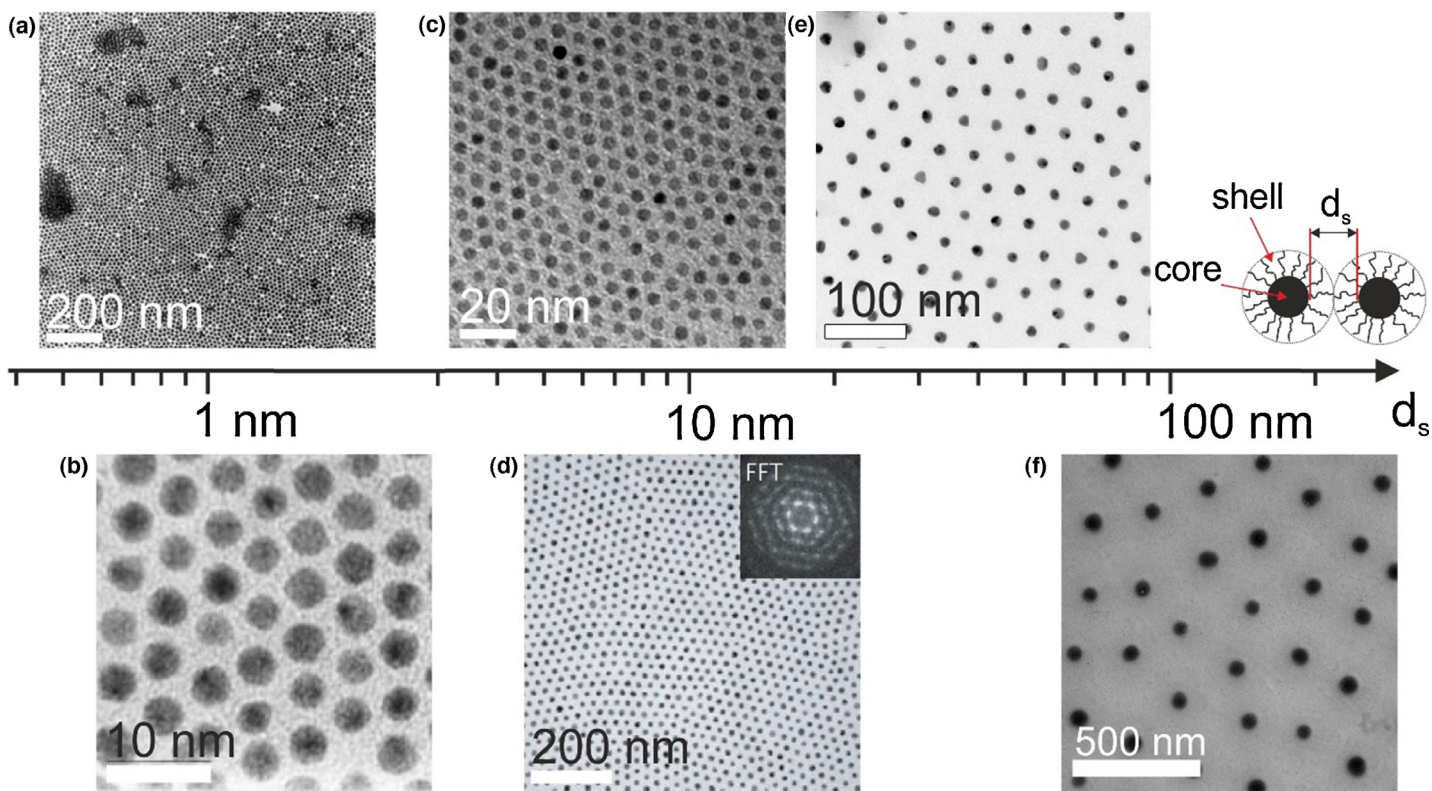
example for this are silica-coated gold nanoparticles [109]. The silica shells cause only slight changes of the optical properties of the gold cores but prevent direct contact of the gold particles in assembled structures, which would significantly change the absorption of the particles due to plasmon resonance coupling [110]. While the silica coating strategy has the advantage of thickness control on the nanometer or even subnanometer scale and it has been adopted to coat also for example anisotropic gold or gold-silver core-shell nanoparticles [111,112], and spherical silver particles [29,113], a disadvantage is the fact that the protocols are usually performed with step-by-step growing of the silica shell. This makes the overgrowth procedure elaborate and time consuming if thick shells are desired. Polymer based materials may have several advantages when used as coating material. Figure 4 gives an overview of inorganic nanoparticles capped by different organic materials enabling a wide range of particle spacings. Very small particle separations  $d_s$  can be achieved when small capping molecules such as citrate (a) [114] or alkyl ammonium molecules (b) [115] are used. In this case values of  $d_s$  in the order of 1 nm can be achieved. This is a separation which is typically much smaller than the diameter of the nanoparticles. The TEM images clearly show that direct contact between the gold nanoparticle surfaces is avoided due to the presence of the shell. Other examples to achieve such small separations are alkyl ligands [116–118], DNA [107,119–122], or short-chain PEG-ligands [123], amongst others. Utilizing larger molecules as ligands gives access to larger  $d_s$ . Figure 4(c,d) shows examples of particle separations in the order of 10 nm achieved by polystyrene (c) [124] and DNA (d) [125]. A further increase in  $d_s$  is possible by increasing the molecular weight of the stabilizing polymer as shown for linear poly-*N*-isopropylacrylamide [126] in Fig. 4(e). Even larger particle separations providing assemblies with lattice constants in the range of the wavelength of visible light are shown in Fig. 4(f). Here an example for hydrogel-coated inorganic nanoparticles (silica) is shown. The concept of hydrogel-encapsulation has been exploited for silica [127,128], gold [129,130], and silver [131] nanoparticles, amongst other materials.

All examples presented in Fig. 4 show that nanoparticles can be well-separated by introducing capping molecules on the nanoparticle surface. The range of possible capping species and their anchoring groups is large and there exist many more systems as presented in Fig. 4. Nevertheless the examples in Fig. 4 nicely demonstrate that separations covering more than two orders of magnitude beginning at nearly atomic dimensions are possible using organic shells.

Once the substrate is covered with colloidal particles with specific inter-particle spacing, surface coverage determines the optical properties, that is, absorption, scattering and transmission [132–135]. Whereas a low area fraction  $\phi_{area}$  of only a few percent will only have negligible influence, a high area fraction will for example significantly lower the transmission through this layer. The maximum area fraction for monodisperse spheres (close-packing) can be calculated as follows:

$$\phi_{area} = \frac{\pi \cdot R^2}{2 \cdot R \cdot \sqrt{3/4 \cdot (2 \cdot R)^2}} = \frac{\pi}{2 \cdot \sqrt{3}} = 0.91 \quad (2)$$

Here,  $R$  is the sphere radius ( $R = D/2$ ). It is obvious that controlling the surface coverage is one of the key challenges for the

**FIGURE 4**

Different strategies of controlling inter-particle distance  $d_s$  between colloidal particles. (a) Au nanoparticles stabilized with citrate leading to an inter-particle separation much smaller than the particle diameter [114]. (b) Au nanoparticles coated with trialkyl ammonium bromide providing particle separations in the order of 1 nm [115]. (c) Particle separation of 7.2 nm obtained through ligand exchange on iron oxide nanoparticles (about 5 nm in diameter) using polystyrene ligands [124]. The spacing between particles can be increased by using higher molecular weight polystyrene ligands. (d) DNA-protected gold nanoparticles with approximately 10 nm inter-particle spacing and fast Fourier transform (FFT) as inset [125]. (e) Linear poly-*N*-isopropylacrylamide ligands on gold nanoparticles give access to particle separations in the range of 12–41 nm [126]. Large particle separation, in the order of the wavelength of visible light, obtained through cross-linked hydrogel shells. Particle spacings in the order of 200 nm were obtained for silica nanoparticles (about 70 nm in diameter) coated with cross-linked poly-*N*-isopropylacrylamide. Note that the organic shells in all TEM images shown here are almost not visible due to the rather large difference in contrast between the inorganic cores and the organic shells. © (a,b,f,e) American Chemical Society, (c) John Wiley and Sons, (d) Nature Publishing Group.

implementation of colloids in PV. Besides the direct influence of the surface coverage on the absorption, scattering and transmission properties, the cost of the colloidal material will require the use of the least amount of material as possible. Thus, a tradeoff exists between reducing the amount of colloids limiting production costs but at the same time to implement enough material to achieve an optical effect.

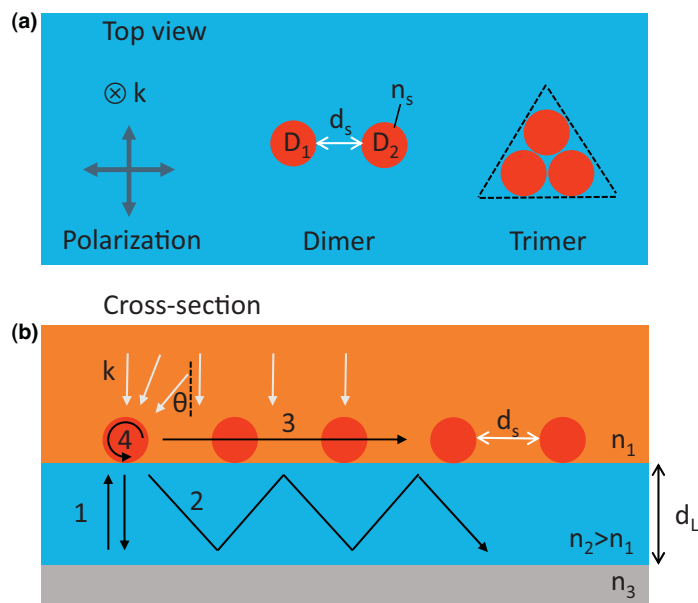
Furthermore, the optical performance of a colloidal monolayer is strongly influenced by the inter-particle separation, that is, the spacing between neighboring colloids  $d_s$ . The spacing  $d_s$  can be directly correlated with the surface coverage for a 2D monolayer with hexagonal packing:

$$d_s = 2 \cdot R \cdot \left( \sqrt{\frac{0.91}{\phi_{area}}} - 1 \right) \quad (3)$$

For example a perfect hexagonal monolayer of spheres with  $R = 50$  nm and an area fraction  $\phi_{area} = 0.5$  will have a spacing of  $d_s = 35$  nm. There are in principle two ways to control the area fraction of particles in a monolayer: (1) through the design of colloidal building blocks, that is, introducing ligands/shells surrounding the particles. (2) Through the assembly process.

Apart from the optical performance, it is also important to consider the electrical and chemical changes of an interface when a colloidal monolayer is applied. Otherwise, for example, the consequences for the charge transport can be severe. Yoon et al. deposited a monolayer of 4 nm Ag nanoparticles right between PEDOT:PSS and the photoactive layer [45]. Indeed, an enhanced absorption was obtained and the  $J_{sc}$  increased accordingly from 6.2 mA/cm<sup>2</sup> (no Ag nanoparticles) to 7.0 mA/cm<sup>2</sup>. However, the fill factor and open-circuit Voltage ( $V_{oc}$ ) decreased significantly, which resulted overall in a reduced PCE of 1.2% compared to 2.2% of the reference cell. This clearly demonstrates the need to adjust optical and electrical properties simultaneously in order to achieve an overall improvement.

Summarizing, controlled surface modification is essential for compatibilization of particles with the PV environment and even allows controlling inter-particle distances and thus gives a handle on tailored surface coverage. Whereas optical properties of randomly distributed particles with large inter-particle distances are additive, additional effects emerge, if the particles are distributed in a periodic fashion and/or show small inter-particle separations. This will be discussed in the following section.

**FIGURE 5**

Schematics of colloidal thin film solar cell light management. (a) Dimer and trimer colloidal assemblies for broadband light absorption ( $D$ : sphere diameter,  $d_s$ : inter-particle spacing,  $n_s$ : refractive index of particle,  $k$ : wave vector). (b) Light-tapping principles and collective optical resonances, such as: Fabry–Perot resonance (1), guided resonance (2), grating coupling (3), and Whispering gallery modes (4). Refractive indices of the different layers:  $n_1$ : dielectric,  $n_2$ : active medium,  $n_3$ : back electrode ( $d_s$ : inter-particle spacing,  $d_L$ : layer thickness). For PV application optical resonances should cover additionally a broad angle of incidence ( $\theta$ ).

### Local and collective coupling effects

Beyond tailoring optical properties of particles on the single particle level, coupling effects between multiple particles open an exciting way of tuning scattering and absorption. Here, we distinguish between local coupling effects and collective effects that require long range order. For simplicity, we discuss only spherical colloidal particles, but the concepts can be extended to particles with less symmetry axes such as rods or cubes [136,137].

Bringing two particles in close proximity has a significant effect on the particles scattering performance and their near-field because of local coupling effects. Figure 5(a) shows a schematic of a dimer assembly with the refractive index of the sphere ( $n_s$ ), sphere diameters ( $D_1, D_2$ ), and inter-particle spacing ( $d_s$ ) located on top of a PV. The refractive index of the sphere should be chosen differently to the environment to have control over scattering, absorption, and enhancement. A simple way to cover the full solar spectrum and to avoid strong polarization effects is to choose different diameters of the spheres ( $D_1 > D_2$ ) or to assemble the colloids into more complex structures like trimers. The inter-particle spacing can be controlled experimentally over a wide distance range with particle surface modifications as has been shown in the previous section ‘Particle functionalization’. The blue shift of the plasmonic resonance in Fig. 2(d) follows a universal scaling law called the plasmon ruler model, which is approximately proportional to an increase of the inter-particle spacing scaled by the diameter [138]. Due to the low near-field enhancement for particles from dielectric and semiconductor materials, additional collective light management is important to give control over the absorption.

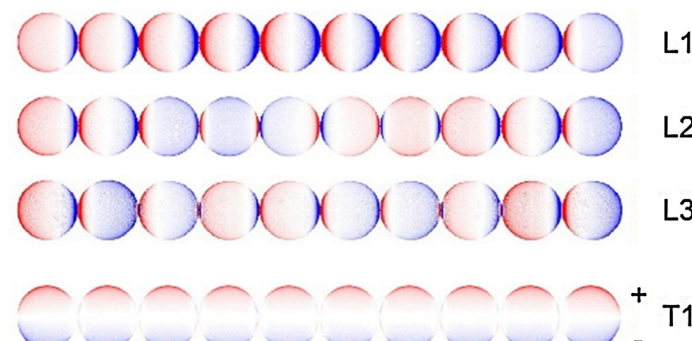
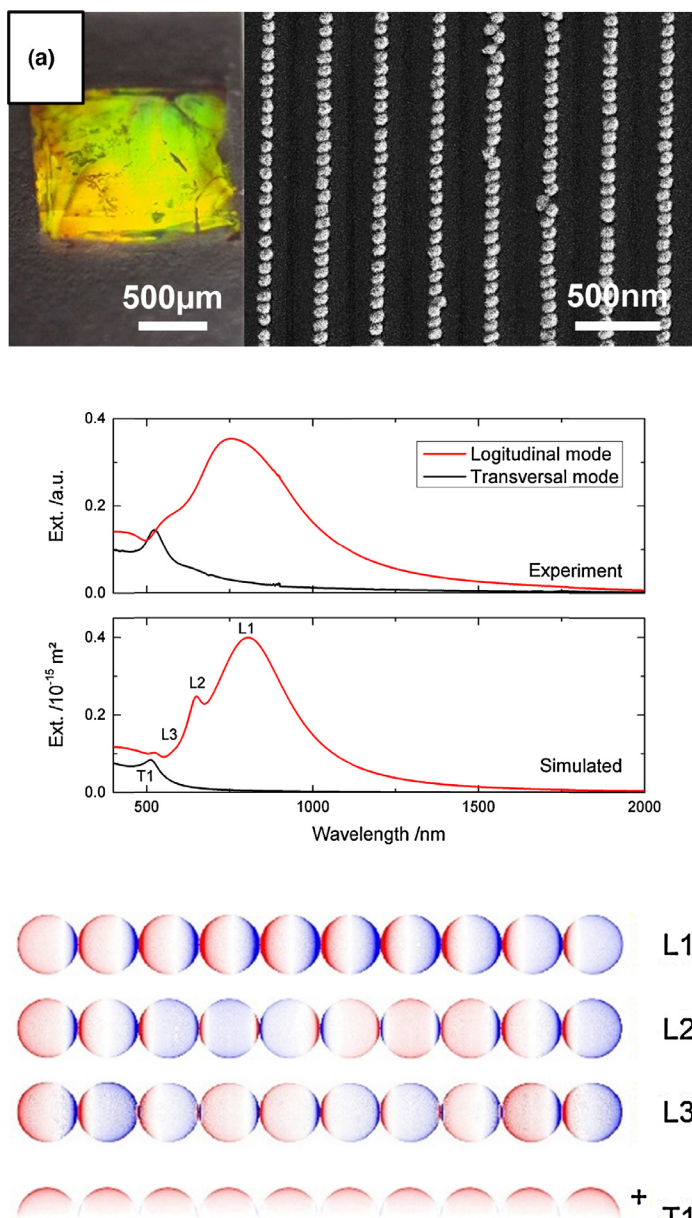
Collective coupling effects are frequently exploited for light trapping. The most important light trapping geometries are summarized in Fig. 5(b), which are addressed for spherical particles (refractive index particle,  $n_s$ : dielectric, semiconductor, or metallic). Initially, we discuss the three light-trapping principles depending on the location of the particle assembly (in the front, embedded into, or on the back electrode) by the specific choice of the layer refractive index  $n_1$ ,  $n_2$ , and  $n_3$  and the position of the colloids inside the optical setup: First, light trapping inside the active layer ( $n_1 = n_2$ ), which results in a close contact of the excited near-field to the active layer [139]. With homogenous surrounding refractive indices the near-field intensity is equally distributed as shown in Fig. 2c. Second, the particles could be used as scattering elements with a radiation pattern pointing toward the active layer ( $n_1 = \text{air}$ ,  $n_2 = \text{active layer}$ ) [24,140]. Third, light trapping can be achieved by a corrugated or periodically structured back electrode ( $n_1 = n_2$ : active layer,  $n_3 = n_s$ ,  $d_L = 0$ ) [141–143].

In terms of the nature of the collective optical resonance, the following scenarios are predominant. The colloidal building blocks and the active layer must have a high refractive index ( $n_s = n_2 > n_1$ : semiconductor materials) in comparison to their environment ( $n_1$ : dielectric) and must have a back mirror ( $n_3$ : metal) [21]. In Fig. 5(b) we show the four most common modes, which could enhance light absorption in the spectral region for solar cell applications: (1) a Fabry–Perot standing-wave resonance [10,21,144], (2) guided resonance of the semiconductor material [145–147], (3) grating coupling along the periodic structure [148,149], and (4) Whispering gallery mode when a wavelength-scale dielectric sphere is in close contact to a high-index substrate [77,150]. These modes or a combination of them, which leads to hybridization, can occur in thin film solar cells. Particularly important are Fabry–Perot resonances, guided resonances and grating coupling structures, for the use in broadband absorption applications. They may also be employed in situations, where the incident light covers a wide angular range relative to the PV device. A further promising route to enhance the optical absorption is to separate the metallic particles with a thin dielectric layer ( $n_2$ ,  $d_L = 3–10$  nm) from the back electrode ( $n_s, n_3$ : metallic), in analogy to the light trapping by periodic structures. This metal–insulator–metal system gives control over the electric and magnetic component to form an ideal absorber [151,152].

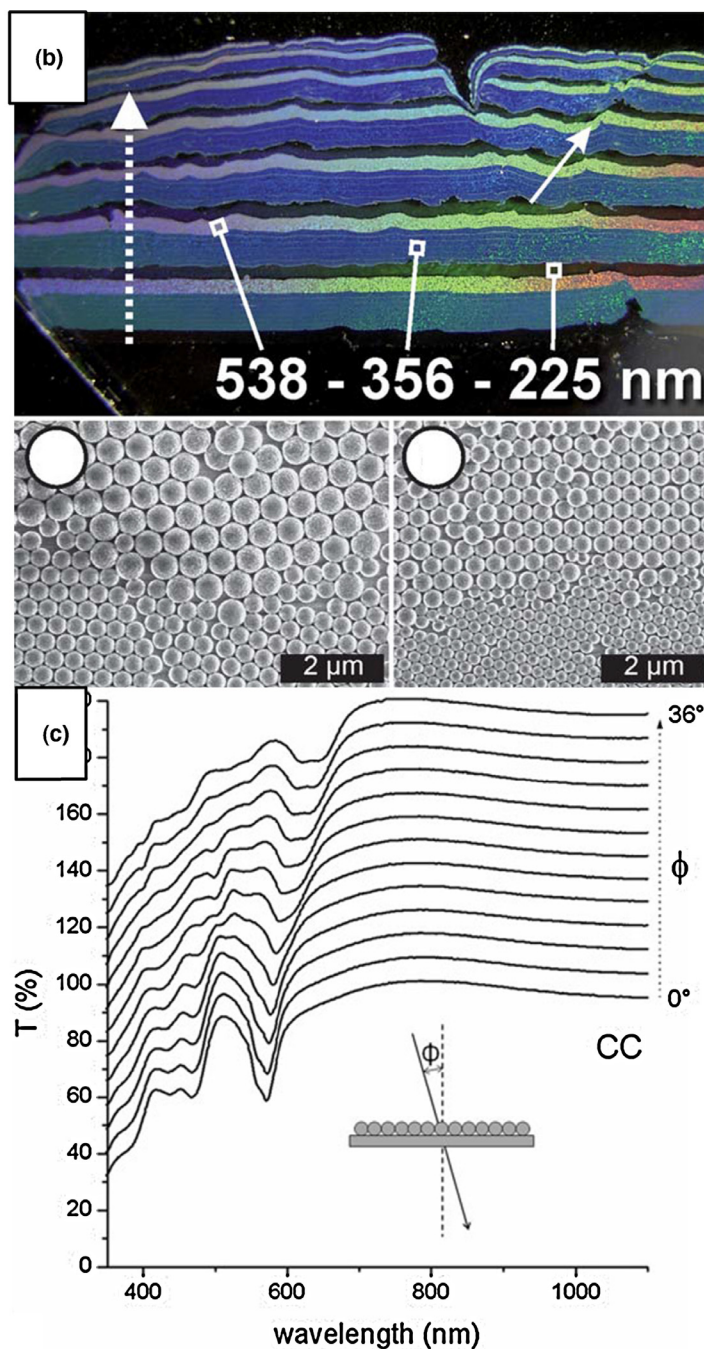
In order to achieve the structural features necessary for the local and collective effects mentioned above, excellent control over inter-particle spacing and/or long range order are required. In the following we review methods that allow for large area fabrication of such ordered structures.

Light absorption enhancement with colloidal assemblies is possible with a simple array fabrication method, which is easily scalable without the need of lithography [153]. Moving from a random particle monolayer to a monolayer of high symmetry such as the hexagonal monolayer schematically depicted in Fig. 1(c), strong interaction with light in the visible or IR region occurs if the periodicity  $l$  is in the order of the wavelength of the incident light due to grating diffraction. Furthermore, the spherical symmetry of the colloids makes it naturally possible to accept a large angle of incidence. Recent studies from Pastorelli et al. made a first attempt into using colloidal assemblies randomly aligned with 1 nm spacing, which show an improvement of their short circuit current by

more than 12% [42]. A step further was done by using assemblies with different particle sizes (core-satellite plasmonic nanostructure), which are linked with a DNA-directed self-assembly process on the substrate as Zheng et al. showed [154]. Consequently, the assembly of different particle sizes (core-satellite plasmonic nanostructure) or particle cluster assemblies [155,156] (trimer in Fig. 5(a) with constant size) are of particular importance for light absorption of a broad frequency range and for the polarization independence because of their structural symmetry [49].



**Figure 6(a)** shows an experimental approach for a particle line assembly, which is fabricated with a lithography free stamp technique [157–159]. This template assisted assembly method makes a centimeter scaled alignment possible with a defined inter-particle spacing and defined orientation of the particles. Furthermore, the modification of BSA coating (Fig. 4) allowed an ultra-small gap spacing (<2 nm) with a low defect rate. This large area precision could be seen in the optical response and in the corresponding modeled spectra. Depending on the polarization a great diversity

**FIGURE 6**

Excitation of optical resonances for periodically arranged colloidal particles. (a) Experimental realization of nanoparticle chains by wet contact printing at different magnifications. Measured and modeled extinction cross-section of the gold nanoparticle lines. Nature of the propagating plasmonic modes (red positive and blue negative charge). (b) Optical micrographs and SEM images of different assembled colloidal particles on a two-dimensional hexagonal lattice [160]. (c) Transmission spectra of a colloidal monolayer with variation of the angle of incidence [161]. © (b) Royal Society of Chemistry, (c) Springer.

of optical modes could be excited, namely (super-, sup-, and sub-sub-) radiant modes (L1–L3) and one dipolar mode (T1) [58]. All of these modes demonstrate the extent of spectral fine-tuning, which is provided by arranging simple colloidal building blocks on an additional hierarchical level. These effects may be used in the future to excite specific modes as outlined in Fig. 5(b) for enhanced absorption.

Another way of template-free structuring and to control the transmission is shown in Fig. 6(b) and 6(c). With a simple inkjet printing approach a monolayer of a hexagonally ordered pattern could be fabricated on various length scales of tens of  $\mu\text{m}$  comprising particles of various size in the visible regime [160]. The reflectance of such long range ordered colloidal monolayers changes accordingly and the effect can be recognized with the bare eye. The transmission properties of such close-packed colloidal monolayers under variation of the angle of incidence is shown in Fig. 6(c). The minimum in the transmission spectrum is associated to light diffraction parallel to the lattice surface (Wood's anomaly), which propagative modes are tunable with the angle of incidence [161].

In close contact with the active layer of a solar cell, such readily assembled dielectric nanospheres can be used to convert the freely propagating sunlight into energy. Figure 7(a) shows a theoretical approach of wavelength-scaled dielectric spheres, which enhance the solar cell efficiency [77] via excitation of whispering gallery and waveguide modes. This study also demonstrated the power to

specifically tune the spectral response by colloidal design. Both particle diameter and particle spacing can be used to enhance absorption in the a-Si layer and thereby increase the current density. Furthermore, this improvement is retained at various angles of incident light, but features some dependence on the polarization of the light. An experimental twist to this concept has been realized by spherical silicon nanoshell arrays by Yao et al. (Fig. 7(b)) [150]. In this experimental study the shell material itself constituted the active (nc-Si) material. The excitation of whispering gallery modes along this shell structure increased the optical path length from 50 nm (planar reference) to 1000 nm. In combination with coupling between adjacent spheres and different particle sizes, an enhanced broadband absorption could be realized. Whereas these structures help to enhance the optical absorption in particular for wavelengths beyond 500 nm, the major challenge is to ensure good electrical contact to guarantee a high open-circuit voltage and short-circuit current density.

Optical light-trapping geometries and optical resonances discussed here are not only restricted to colloidal particles. The optical principles can be expanded to inverted structures such as periodic hole structures (part 2). This relation expressed in the Babinet's principle, which yields a correlation between the diffracted light of an opaque mask and the inverted structure. This principle was originally used to simplify the analysis of diffraction problems [162].

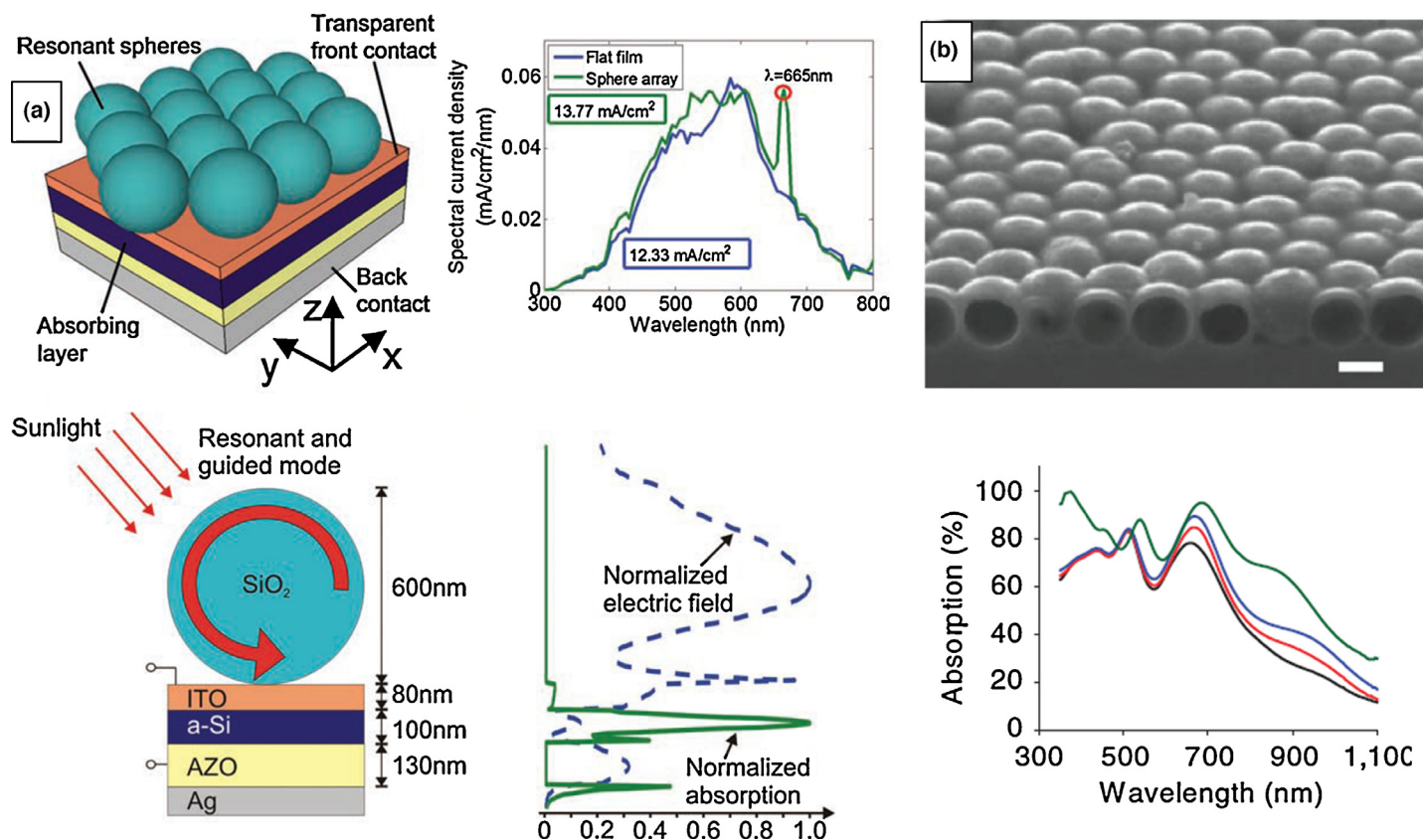


FIGURE 7

Using wavelength-scale dielectric sphere assembly to enhance solar cell efficiency. (a) Schematic for resonant coupling by a dielectric sphere in close contact to a high-index PV absorber layer (whispering gallery modes). Adjacent, calculated optical generation rate in the silicon using a flat film or the sphere array. Cross-section of the solar cell device and the normalized integrated electric field and absorption in the respective layer [77]. (b) Cross-section SEM image of a spherical nanoshell monolayer and corresponding absorption spectra (black: one layer, red: two layer, blue: three layer, green: ITO as anti-reflecting coating) [150]. © (a) John Wiley and Sons, (b) Nature Publishing Group.

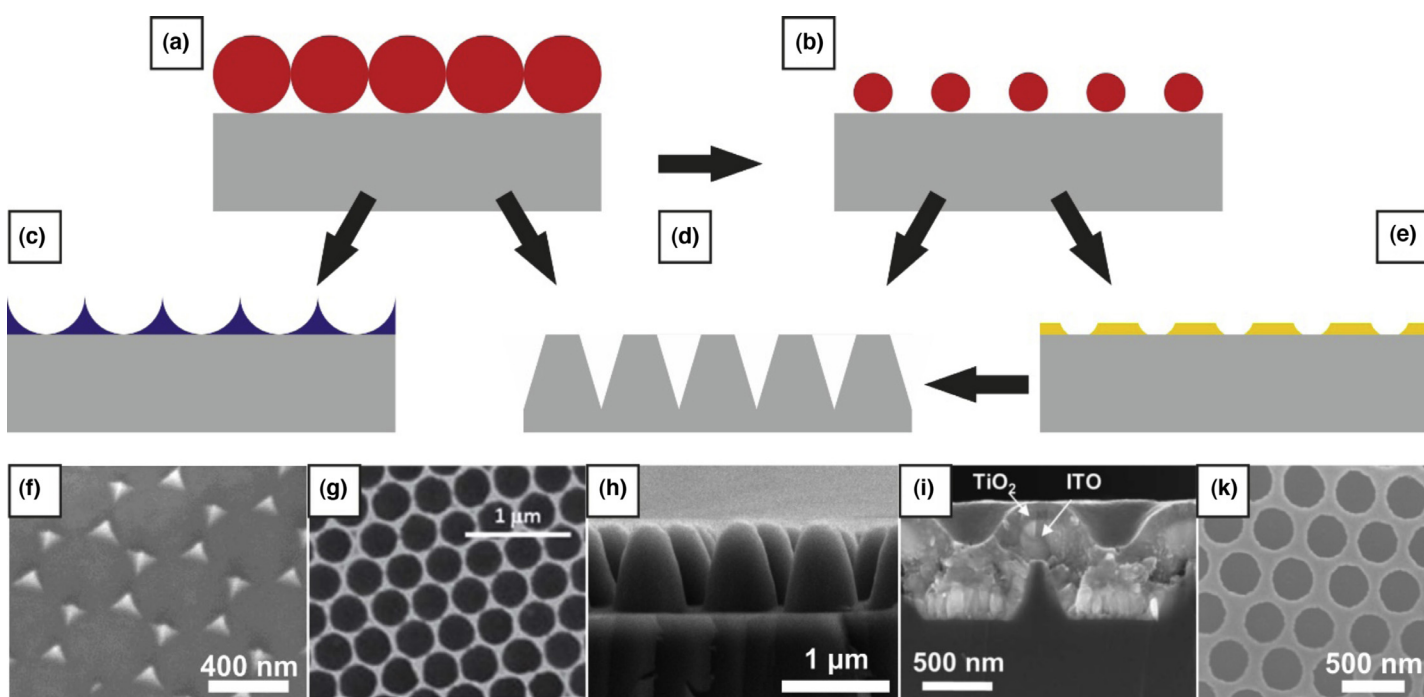
## Template electrodes from colloidal assembly structures

Whereas the last section has discussed the use of assembled colloids as light management structures in PV, a colloidal particle layer can also be used as templating structure for further modification of devices. This concept is typically known as nanosphere lithography. This increases the parameter space compared to colloidal structures discussed before and allows additional design elements in both material and nanostructure to trap light in thin film PV devices. Figure 8 depicts three simple categories of templated electrode designs along with examples from literature. We focus on two-dimensionally ordered particle arrays but note that other assembly structures introduced in the previous sections may also be used for templating purposes. Furthermore, colloidal lithography itself represents a very active field of research, which demonstrated a vast range of possible ordered and non-ordered nano- and mesostructures. For more details on colloidal lithography, we recommend the reader specialized reviews in this field [163,164]. Here, we restrict ourselves to examples from colloidal lithography that made direct contributions to light management or photovoltaics.

The fabrication of templated structures for top or bottom electrodes can either start from close-packed colloidal monolayers (periodicity  $l$  equals particle diameter), or non-close-packed arrays. The latter structures are typically fabricated using an isotropic dry etch process, for instance by plasma etching [170]. Replication of this periodic structure can be conducted with various degrees of complexity. Most straightforward is the deposition of a desired material into the interstitial space of a close-packed monolayer (Fig. 8(a,c)).

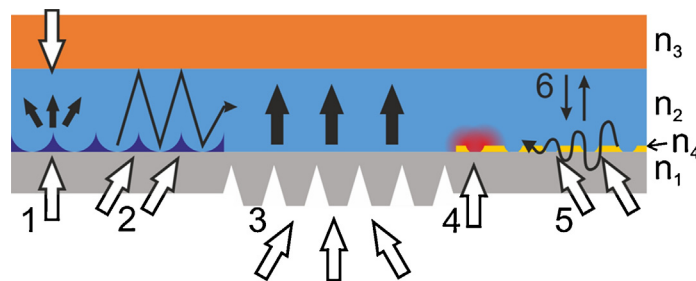
Depending on the amount and height of the added material isolated triangular pyramidal structures (Fig. 8(f)) [165] or nanobowl arrays (Fig. 8(g)) [166,171] are obtained. One can also capitalize on the chemical contrast between the surface and particle array material to transfer the periodic structure into the supporting substrate instead of building it on top (Fig. 8(d,h)) [167]. By proper adjustment of the etching parameters and gas composition the aspect ratio and tapering gradient can be tuned to get nanopillars as well as nanocones from the same starting material. Non-close-packed colloidal monolayers (Fig. 8(b,e)) can be converted into nanomesh structures (Fig. 8(k)) [169]. Most commonly this nanomesh is metallic and can be used as a transparent conducting electrode simultaneously. One can further exploit the contrast in materials chemistry between the nanomesh and support substrate. Similarly to the etching process employed in Fig. 8(h), the nanomesh can serve as a protective layer. Therefore, only the free holes are subjected to the etching process, which yields nanobowls (Fig. 8(i)) or nanowell, which are embossed into the support structure [141,168]. The structural diversity shown in Fig. 8 is not limited to a specific type of material, but can be regarded as generic motif, which in principle can be realized by metals, metaloxides, polymers and graphitic entities.

Concomitant with the structural richness of the templated electrodes, there is a range of optical properties, which can lead to an enhanced performance of the PV device. These include light trapping by scattering, excitation of photonic waveguides, or local field enhancement by plasmonic resonances. Additionally, increased light absorption can be achieved by the antireflective properties in particular of tapered nanocones and by an angle-independent



**FIGURE 8**

(a) A close-packed colloidal monolayer is immobilized on a substrate. The spheres typically consist of polystyrene (PS) or silica. (b) Isotropic etching reduces the particle size but retains the initial periodicity. (c–e) A range of templated motifs is accessible: Isolated pyramids or continuous bowl-like films remain after direct deposition through the orifices (fg) [165,166]. Exposing a colloidal monolayer to reactive ion etching yields nanopillars, nanodomes, and nanocones depending on the respective etching rates (h) [167]. Multiple layers of photoactive and electrode material can be constructed on top of a templated substrate (i) [168]. Etched colloidal monolayers can be coated with various metals resulting in mesh-like structures, which act as conducting electrodes themselves (k) [169]. © (f) AIP Publishing LLC, (g) Royal Society of Chemistry, (h) IOP PUBLISHING, LTD, (i) Nature Publishing Group. (k) AIP Publishing LLC.

**FIGURE 9**

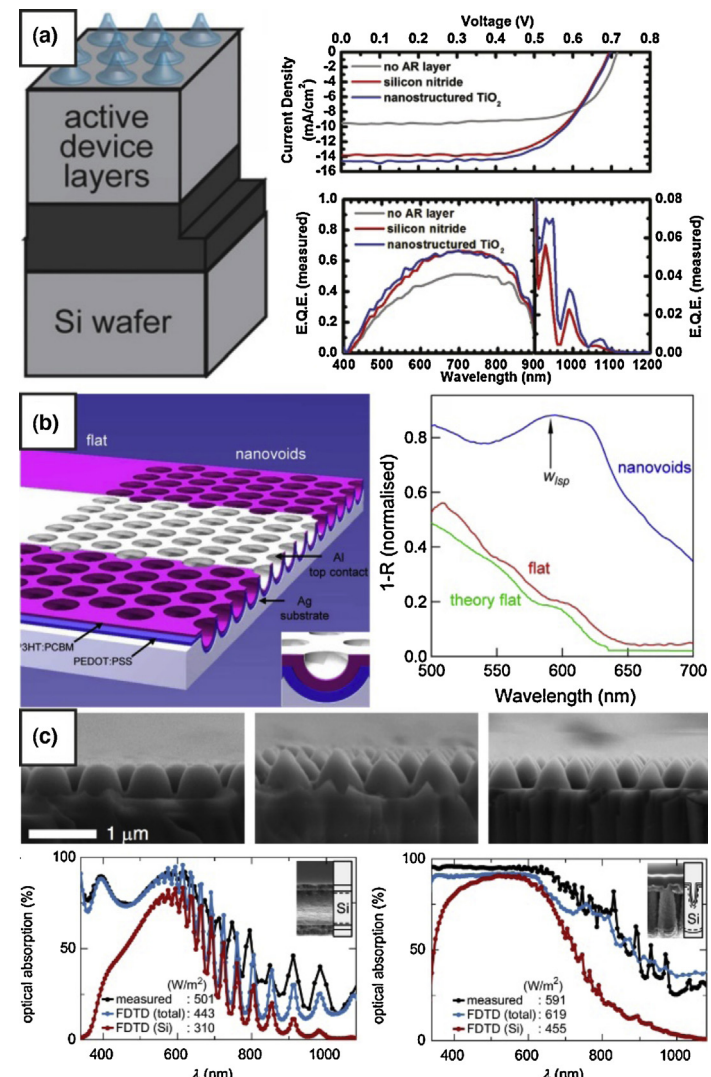
Schematic of optical properties of colloidally templated electrodes.  $n$  denotes refractive indices:  $n_1$  is typically glass (front or top electrode),  $n_2$  the photoactive layer,  $n_3$  the counter electrode often a metal (back or bottom electrode), and  $n_4$  the templated structure. White arrows indicate incident light, black arrows the light after passing the templated structure. (1) (back)scattering of light, (2) excitation of photonic waveguide modes in the active layer by grating coupling, (3) antireflective properties of graded interfaces and angle-independence of light transmission (4) excitation of localized surface plasmons, (5) excitation of propagating surface plasmons, (6) excitation of cavity modes.

absorption. Continuous metallic nanostructures cannot only be employed as a conducting electrode but may also be able to support propagating surface plasmons. These optical contributions are schematically summarized in Fig. 9. Furthermore, when using these structures as electrode material, the interfacial contact area to the photoactive layer is increased compared to the analog flat structure allowing for an increased charge carrier extraction.

In the following we will discuss a range of nanostructured electrodes, which can be derived by colloidal lithography strategies as outlined in Fig. 8. For reasons of clarity, we refer to 'front' or 'top' electrode when the electrode is (semi)transparent and faces the direction of illumination. We will refer to 'back' or 'bottom' electrode for the non-transparent electrode.

#### *Structured electrodes from close-packed colloidal monolayers*

Following route c from Fig. 8 allows one to fabricate insulated structures, which typically possess a pyramidal shape with a triangular base. In this context insulated means on the one hand a spatial separation that can be adjusted by the templating colloidal array (via  $l$ ). On the other hand these structures are also electrically non-continuous requiring an additional electric contact to provide charge carrier extraction. Sputtering or evaporation techniques can be used to obtain defined individual structures of a certain height. Li et al. sputtered  $\text{TiO}_2$  onto a colloidal monolayer comprising 500 nm diameter polystyrene beads. These high refractive index structures of 250 nm in height on top of an As/GaAs multiple quantum well solar cell fulfilled two purposes: broadband antireflective properties and excitation of waveguide modes into the quantum well layer. The advantage of the nanostructure over a flat layer antireflective coating is a higher light transmission for wavelengths below 600 nm and the additional excitation of optical waveguide modes above 900 nm, which both result in a higher  $J_{sc}$ , as can be seen in Fig. 10(a) (bottom right). Furthermore, the nanostructured devices featured a strongly reduced sensitivity toward the angle of illumination, particularly for short wavelengths ( $<600$  nm), which is important for non-tracking solar devices. However, the benefits gained from an increased absorption in the active layer are compromised by a concomitant

**FIGURE 10**

(a) Sputtered  $\text{TiO}_2$  nanopyramids on top of a thin film quantum well solar cell. A combination of antireflective coating and waveguide excitation in the active layer increases the  $J_{sc}$  compared to the flat structure or conventional unstructured AR coatings. Alongside, the EQE is increased [165]. (b) Thin film P3HT/PCBM solar cell on top of a nanobowl Ag bottom electrode. Local and surface plasmon enhancement increases the absorption in the active layer [174]. (c) Direct etching of nanocones into a glass substrate. The absorption in a  $\mu\text{c-Si}$  cell is increased, which critically depends on the periodicity and depth of the etched structure [167]. © (a) AIP Publishing LLC, (b) OSA, (c) IOP Publishing. Reproduced by permission of IOP Publishing. All rights reserved".

increase in surface recombination. Without surface recombination effects short-circuit current densities of up to  $34.9 \text{ mA}/\text{cm}^2$  could be expected instead of  $14.6 \text{ mA}/\text{cm}^2$ , which has been measured in this work (Fig. 10(a) top right).

In the field of nanosphere lithography noble metals have been widely employed as sputtering or evaporation material due to the rich optical properties of the resulting plasmonic nanostructures. Naturally, these motifs have also been investigated for their application in solar cells [172,173]. In contrast to dielectric structures as described above the evaporated layer thicknesses typically range in the few tens of nanometers for gold, silver or aluminum. Therefore the main gain in absorption efficiency is not derived from antireflective properties, but rather local plasmonic field enhancement

or scattering at these structures. Studies by Kirkeminde et al. and Wu et al. on bulk-heterojunction solar cells, both point toward an optical effect caused by plasmonic field enhancement or scattering, as the EQE or incident photon-to-electron conversion efficiency (IPCE) are most enhanced at or close to the plasmonic resonance of these nanostructure [172,173]. When incorporating metallic structures into or close to the photoactive layer, however, one has to prevent adverse effects such as exciton quenching and surface recombination. This can for instance be achieved by passivation of the plasmonic structure with suitable self-assembled monolayers (SAM). A benefit of plasmonic nanostructures obtained by nanosphere lithography lies in the ease of spectral adjustment of the plasmonic resonance by the size of the templating particles as well as the defined high surface coverage and distribution. This periodic distribution may additionally lead to the excitation of photonic waveguide modes in the photoactive layer.

Instead of electrode structuring by evaporation or deposition on top of the colloidal assembly structure, one can also replicate the particle periodicity by a bottom-up growth. In particular electro deposition of metals such as Ag [174] or semiconducting polymers such as PEDOT [166] (Fig. 1(g)) were employed to generate nano-bowl-like structures on top of a suitable substrate. For PEDOT nanobowls Wei et al. observed an increase in  $J_{sc}$ , which they assigned to an increased light path in the active layer and the increase in the interfacial area between the active layer and the electrode. No pronounced antireflection effect was observed for this configuration, in which the structured electrode resembled the transparent layer facing the direction of illumination. In the case of Ag nanobowls formed by electrochemical deposition, the nanostructured layer featured the bottom electrode at which the incoming light was back reflected into the photoactive layer (Fig. 10(b)). This nanobowl structure contributed to a fourfold increase in total cell efficiency compared to devices using flat electrodes. The authors attributed this increase mainly to a higher absorption in the photoactive layer (Fig. 10(b) right) caused by the strong local field enhancement given by the local surface plasmon resonances that are present in these nanobowl arrays. Further advantages are an increased active semiconductor area and enhanced scattering from the interface. The absolute efficiency of this configuration, however, was only 0.2%. The main losses occur at the front electrode, which was a 15 nm Al layer. The corrugation of this electrode may additionally increase the electrical resistance, which resulted in a decreased fill factor. Lal et al. expanded their investigation on such regular nanovoids to randomly structured glass electrodes (Asahi glass) and determined the influence of the spacer layer between the Ag electrode and the photoactive layer [175]. Quite importantly, they found that the thickness of the spacer layer represents a critical design parameter, which greatly depends on the actual photoactive material. For low-n photoactive materials such as organic solar cells a thin spacer layer (few tens of nm) is recommended in order to make use of the plasmonic near-field enhancement. For high-n materials such as  $\mu$ -Si solar cells, a thicker spacer layer can suppress absorption in the metal layer but allow for guided modes being scattered into the active layer.

Instead of widely used spherical polymer particles, Xie et al. have very recently shown that also gold nanowires can be used to transfer a predefined topography into a designated electrode material. In their particular case they have used very high aspect ratio

wires for texturing of ITO electrodes on silicon solar cells [176]. The wires were preassembled using a Langmuir Blodgett technique resulting in a wrinkled interface. Sandwiching these between the ITO electrode and the single crystalline silicon solar cell yielded a 13% increase in  $J_{sc}$  which has been mainly rationalized by a decreased reflection at the Si/ITO interface. This example shows that apart from polymer particles also other colloidal materials can be successfully employed for electrode texturing.

Taking advantage of the material contrast between a polymeric colloidal monolayer and a glass or silicon substrate textured surfaces with nanocones and nanopillars of various shapes can be fabricated (Fig. 10(c) top row). The etching depth and shape can be adjusted by the etching time and composition of the reactive gas, most commonly  $CH_3F$  and  $O_2$ , respectively. This method can be directly applied to a thin-film silicon solar cell [177]. The gradual change in refractive index for the case of Si-nanocones as interface to the air demonstrated the highest absorption in combination with a very low dependence on the angle of illumination. This kind of gradual nanostructures can also be used to construct a PV cell on top, with the nanopillars either being the top or bottom electrode. An example of a transparent top electrode was investigated by Mailoa et al. [167]. They deposited conformal layers of AZO (aluminum-doped ZnO) as transparent conducting electrode and  $\mu$ -Si as photoactive layer. Similar to the case of nanopyramidal  $TiO_2$  structures as discussed above, such nanoconical grooves decrease the reflection at low wavelengths and increase the scattering into the photoactive layer at longer wavelengths (Fig. 8(c) bottom row). The periodicity and height of these nanostructures has a distinct influence on the total absorption of the fully assembled device. Optimum parameters for their particular study were about 900 nm in periodicity and 900–1300 nm in height. The  $J_{sc}$  increased in this case from 15.0  $mA/cm^2$  (flat cell) to 21.6  $mA/cm^2$  (nanocone device), which is an increase of 29% relative to a state-of-the-art textured reference cell. Further improvements need to be done electrically, in order to reduce shunting in the nanotextured devices. Starting from the same structured electrode material Zhu et al. fabricated a p-i-n a-Si:H solar cell on top, with the textured glass substrate being the bottom electrode in this case, coated with a 100 nm thick layer of Ag as back reflector [178]. The multilayer structure was applied conformally such that the corrugation was retained in the final device. Essentially the same optical behavior has been observed as discussed before, namely a reduction in reflectance at the top device-air surface and an increased absorption at longer wavelengths, both leading to a higher  $J_{sc}$  (17.5  $mA/cm^2$  for the nanostructure compared to 11.4  $mA/cm^2$  for the flat reference). The efficiency increased from 4.7% to 5.9% and was less sensitive to the angle of illumination. The texture of this surface has been further used in this study to investigate self-cleaning properties of such a device. After fluorination with a perfluoroctyl trichlorosilane a water contact angle of 141° was measured, which was large enough to remove adsorbed dust particles by simply rinsing with water. Therefore, such nanostructured devices may offer further multifunctional advantages compared to their flat cell analogs.

#### *Structured electrodes from non-close-packed colloidal monolayers*

Let us now turn toward structures that can be templated from non-close-packed colloidal monolayers. The most directly templated

structure represents a perforated electrode, which typically comprises Au, Ag or Al as deposited material. These perforated metals (often referred to as nanomeshes or nanohole arrays) can be used as a replacement for ITO as a transparent conducting electrode (TCO). A lot of research has been devoted to the physics of light transmission in the near-field and far field of such nanosized apertures [179,180]. Here we want to restrict the discussion to systems that have been implemented in actual PV devices.

Nanomesh structures can be further divided into random hole ensembles and periodic arrays. Random ensembles are typically fabricated by electrostatic adsorption of colloidal particles onto an oppositely charged substrate, in most cases glass. The degree of particle coverage can be controlled by adjustment of the Debye screening length for instance via different ionic strength in the dispersion medium [181]. Reilly et al. compared P3HT/PCBM solar cells on top of either ITO as reference, on top of an Ag film or on an Ag random nanohole array [182]. The optical transmission was highest for the ITO electrode, which also resulted in the highest efficiency of 3.68%, whereas the Ag film with 30 nm thickness featured only 1.03%. The introduction of nanoholes of 92 nm and 350 nm diameter with a surface coverage of ~0.2 increased the efficiency slightly to 1.18% and 1.22%, respectively. The introduction of nanoholes in the Ag film not only increases the transmission of light, but also leads to the excitation of local surface plasmons in these orifices and propagating surface plasmons at the metal/active layer interface, which can trap light and generate enhanced local fields. The surface coverage of random hole arrays is limited to about 0.4 in order to ensure electric conduction, which can be described by a percolation model. If higher surface coverage is desired, hexagonally ordered arrays are needed. These can be achieved from close-packed spheres, which will be reduced in size by a suitable post-treatment after assembly [183].

Such periodically structured electrodes covering a range of different length scales were investigated by Zhu et al. [169], Morfa et al. [184], and Luhmann et al. [185]. The results draw a heterogeneous picture of whether such structured electrodes can be used as efficient replacement of state-of-the-art ITO electrodes. In the case of Luhmann et al. thin patterned Ag electrodes with thicknesses ranging from 12 nm to 20 nm were investigated with a periodicity of 400 nm and hole sizes from 175 nm till 250 nm. Whereas the transmission through such nanomeshes is greatly reduced compared to ITO, the power conversion efficiency turned out to be larger using a CuPc (Copper phthalocyanine)/C<sub>60</sub> active layer. This increase can again be understood by the excitation of plasmonic resonances, which increase the field intensity in the organic layer. For the sizes and spacing investigated by Luhmann et al. this effect was most pronounced for wavelengths >550 nm, which became apparent in EQE measurements. Zhu et al. investigated an organic solar cell comprising P3HT/PCBM on top of a nanomesh electrode with a PEDOT/PSS spacer layer between the electrode and the photoactive layer. The nanomesh featured a 430 nm periodicity and a hole diameter of 357 nm along with a 18 nm thick Au layer. Similar to Luhmann et al., the optical transmission for this system was reduced compared to ITO. In addition, the overall power conversion efficiency was also slightly lower since most of the plasmonic field enhancement was confined to the PEDOT:PSS layer and not significantly affecting the active layer. Still a considerable PCE of 3.12% could be obtained.

The authors further demonstrated the tuneability of the optical properties of such nanomesh films by adjustment of the periodicity, aperture diameter, and metal film thickness (Fig. 10(a), right). These parameters allow for tuning the spectral modes over a wide range of the visible wavelength regime. This allows for straightforward fine tuning of the optical properties with respect to the photoactive layer. Morfa et al. determined the properties of nanomeshes with a rather large (756 nm) periodicity and concomitantly large hole apertures consisting of Ag films with 50 nm thickness. Neglecting contributions from local or propagating surface plasmons, which play a minor role for this size regime, they particularly investigated the interplay of the overall transmission along with the sheet resistance and resistive losses of such large nanomeshes. These typically follow opposite trends, with large hole diameters and a high optical transmission having higher electrical losses due to an increased sheet resistance. The PCE of the ITO reference therefore always outperformed the Ag nanomesh devices in the case of P3HT/PCBM organic solar cells.

It becomes apparent from these studies that there is no simple replacement of ITO by perforated metal electrodes, but that these systems need to be carefully adjusted and optimized, both optically and electrically in order to obtain an increase in efficiency, which justifies the added complexity of the fabrication process.

The properties of solar cells with a metallic nanomesh as front-electrode critically depend on the fine-tuning of (1) the nanomesh characteristics (periodicity, metal type and thickness, which govern optical and electrical properties), (2) the blocking and active layers (thickness, refractive index, band gaps, electric resistivity), (3) the back electrode (work function, sheet resistance).

Some of these properties were investigated in a recent study by Chou et al. [186], where a range of P3HT/PCBM device configurations was tested on top of square hole arrays fabricated by nanoimprint lithography. Their optimized device configuration featured a 30 nm thick gold mesh (hole array of 175 nm diameter and 200 nm periodicity) on a fused silica substrate, 10 nm thick PEDOT:PSS electron blocking layer, 85 nm P3HT/PCBM active layer, 5 nm thick TiO<sub>x</sub> hole blocking layer and a 100 nm thick Al back electrode. This device provided a PCE of 4.4% in contrast to the ITO reference of 2.9% (with the same layer thicknesses). The reason for this strong enhancement stems from the high EQE of the plasmonic nanomesh device of up to 69%, which is remarkable for an active layer thickness of only 85 nm. This could be explained by a reduced reflectance (Fig. 11(b) left) and an increased absorption (Fig. 11(b) right) of the nanomesh device compared to the ITO reference. Even more intriguing are the changes observed, when comparing the optical properties of the individual nanomesh with the final assembled solar cell. Chou et al. found a decrease in reflectivity and absorption of the nanomesh layer after the solar cell was assembled with Al as back electrode. They attributed this effect to a plasmonic cavity effect between the nanomesh and the Al back electrode, which leads to efficient light coupling and trapping into the active layer. On the front nanomesh electrode the incoming light excites plasmonic resonances. According to the authors, the resulting evanescent waves can couple into the back metal layer, given the separation distance (i.e. the cavity length) is not too large. Furthermore, these nanomesh devices exhibited a lower efficiency dependence with respect to the illumination angle compared to the ITO reference.

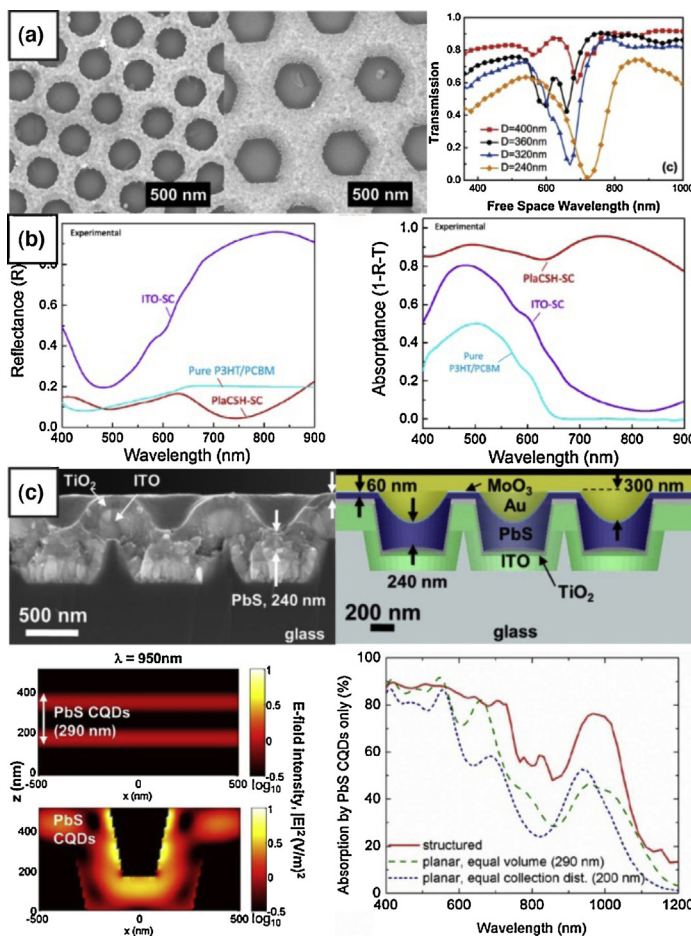


FIGURE 11

(a) Perforated metallic electrodes can be tuned in periodicity  $\lambda$  and hole diameter by the constituting particle monolayer and etching conditions. Metallic nanomeshes feature distinct resonances and simultaneously replace ITO as transparent electrode material [169]. (b) The reflectance decreases, the absorptance increases for gold nanomeshes with a square symmetry compared to the ITO analog. In combination with an increased light trapping, nanohole electrodes outperform the ITO analog [186]. (c) Metallic nanomeshes were used to transfer holes of defined periodicity into a glass substrate. After sputtering with ITO the nanostructured glass was used as top electrode support for the deposition of a quantum dot solar cell. The deposition of Au into such nanowells lead to local field enhancement and power absorption. Therefore a broadband absorption increase and reflection suppression could be observed optically, which translates into an overall increased conversion efficiency [168]. © (a) AIP Publishing LLC, (b) OSA, (c) Nature Publishing Group.

All of these examples demonstrate a vast range of optical phenomena that need to be controlled, when using metallic nanomeshes as front electrode. The loss in transmittance needs to be balanced with an increased absorption by light trapping in the active layer, which could be achieved by local or propagating surface plasmons. Furthermore plasmonic cavity effects or photonic waveguide modes may be excited depending on the optical length of the active material. Even more peculiar, the optical properties may change considerably compared to the individual layer structures, when fully assembled into the thin-film device. At the same time these structures need to provide electrical properties, which guarantee low resistivity and losses at the electrode interface.

Metallic nanomeshes also provide an orthogonal materials contrast to the most commonly used glass or silicon substrate. Analogously to the masking properties of polymeric particles, as discussed above for fabrication of nanopillars and nanocones, these nanomeshes can be embossed complementary into the substrate as nanowell. This can for instance be directly applied to Si solar cells [187]. The introduction of nanowell with appropriate periodicity and depth leads to an effective reduction in reflectivity, which is furthermore largely independent of the angle of incidence. The average reflectance (from 400 nm to 1000 nm) could be decreased from 8.6% for the flat reference to 4.7% of the best nanohole device. It is important that defects, which are introduced during the reactive ion etching step are removed by a damage removal etch. This procedure led to a  $J_{sc}$  of 31.5 mA/cm<sup>2</sup> and a power conversion efficiency of 11.9%. Using rigorous coupled-wave analysis (RCWA), the authors also investigated the influence of such nanoholes on the thickness of the Si solar cell. For Si solar cells exceeding 100  $\mu$ m, only a minor enhancement can be expected, but for thinner devices the light trapping in the Si layer can lead to an enhancement of up to 40%. From this analysis the authors conclude that an identical current output can be achieved for a nanohole structured device of 10  $\mu$ m thickness, compared to a flat 200  $\mu$ m Si solar cell, demonstrating the possibility to reduce the material usage by 95%.

Transferring the periodicity of a metallic nanomesh electrode into a glass substrate results in nanobowls or nanoholes depending on the etching depth. These can be used to build PV devices on top, with the nanostructured glass substrate being the front electrode. Battaglia et al. investigated the influence of periodic and random texturing on amorphous hydrogen silicon (a-Si:H) thin film solar cells of only 250 nm thickness. Compared to a flat cell reference the  $J_{sc}$  could be increased from 12.0 mA/cm<sup>2</sup> to 17.1 mA/cm<sup>2</sup> for a 350 nm periodic texture, and the efficiency reached 10.9%. The periodicity increases light absorption in the active layer by scattering into guided optical modes. However, randomly etched structures exhibited almost identical performance properties. Conducting a detailed theoretical study, the authors conclude that periodic structures should outperform random textures optically, as scattering into lossy channels can be avoided. Concomitantly, the electric properties also have to be optimized, in order to retain layer conformality and reduce losses, which would result in reduced  $V_{oc}$  and fill factor (FF).

A more sophisticated multilayer architecture has been investigated by Adachi et al. [168], who fabricated a colloidal quantum dot (CQD) solar cell on top of a nanohole etched glass substrate. The PbS quantum dot layer had a thickness of 60–240 nm, with the variation being due to the non-conformal coating of the nanohole structure, which is shown in Fig. 11(c). The CQD layer was separated by a thin MoO<sub>3</sub> layer (25 nm) from the Au (150 nm) and Ag (240 nm) back electrode contact. The optical properties were investigated by FDTD simulations and revealed two major contributions to an enhanced absorption in the CQD layer: (1) a reduced reflectance below 700 nm allowing for more light to enter the active layer, which is caused by the tapered structuring of the front electrode and (2) electric field enhancement in close vicinity to the Au electrode interface (Fig. 11(c), left bottom). The planar device features interference patterns, whereas the nanostructured electrode leads to local or propagating surface plasmons at the

Au/CQD interface. This enhancement is particularly strong for 600–1200 nm, where the absorption length of the PbS CQDs absorption per unit length is weaker. These effects together result in a superior absorption in the CQD layer compared to the planar reference (Fig. 11(c) right bottom). The experimental realization of this solar cell configuration yielded a  $J_{sc} = 20.2 \text{ mA/cm}^2$  and an efficiency of 6.0% whereas the planar device delivered a  $J_{sc} = 15.2 \text{ mA/cm}^2$  and 5.2% efficiency only.

Summarizing the wide range of PV architectures that can be derived from colloidally templated electrodes, it becomes clear that such approaches can contribute significantly to new light harvesting concepts but also may allow for new device layouts. The physics of efficiency enhancement is by far not limited to a certain type of PV device, but certainly needs to be specifically tailored to the precise application. In this section we introduced examples ranging from (thin film) silicon solar cells, to colloidal quantum dot devices and organic solar cells. Ways of enhancing the power conversion efficiency include:

- (1) Reduced reflectance by gradient structures.
- (2) Absorption increase by scattering into guided modes.
- (3) Absorption increase by field enhancement due to local and propagating surface plasmons.
- (4) Absorption increase by light trapping in the active layer due to photonic and plasmonic cavities.
- (5) Increased performance by omni-directional light trapping into the active layer.
- (6) Increased charge carrier extraction due to an enlarged electrode interface.

When realizing such nanostructures, the optimization of optical and electrical properties has to be equally taken care of. Beyond that, periodic textures can change the wetting properties of the electrode, which can reduce the adsorption of dust and retain the longterm performance. The application of colloidal particles for the fabrication of ultrahydrophobic surfaces has also been demonstrated with hollow silica spheres. These were adsorbed on the top surface of a PV cell and were then passivated with a perfluorosilane. The low refractive index of the hollow spheres did not change the transmission through the glass slide, while rendering the surface ultrahydrophobic due to the increased roughness [188].

Finally, such templated electrode structures are also accessible by other techniques such as nanoimprint lithography. The PDMS stamps, which are typically used in these processes, can be fabricated by lithographically (photolithography [189], interference [186]) structured masters, but also by colloidally assembled structures [190]. This further opens the parameter space of structures and symmetries that can be employed in the improvement of thin-film devices.

## Conclusion

This review is dedicated to colloidal approaches toward light management in PV systems. In the first part, we discussed the general layout of a PV device with colloidal light management structures, where the colloids are either embedded in a homogeneous refractive index environment or close to an interface. In this respect we discussed different effects by which colloids can influence the device performance, namely scattering, absorption and near-field enhancement. The scattering performance of simple

dielectric particles and in addition the absorption and near-field properties of particles with a complex dielectric function were compared on the basis of theoretical simulation and linked to specific examples that illustrate the state of the art of controlling the relevant parameters, namely size, shape and composition. We highlighted synthetic strategies by which tailor-made colloidal objects can be obtained. Building up on this foundation, we focused on the functionalization of particles that ensures colloidal stability, compatibility with the matrix material and offers a convenient way for controlling inter-particle distances and thus surface coverage. Up to now many colloidal monolayers have been prepared in a rather random fashion with little control over the inter-particle distance. Importantly, defined inter-particle distances allow for collective optical effects, which add another dimension for tailoring optical properties of colloidal assemblies. Here local coupling phenomena and collective effects requiring long range order arise. We illustrated assembly strategies for the generation of colloidal monolayer with different structures and discussed these in the light of their relevance for light harvesting. In the second part, we turn our focus toward templating applications of colloidal particles. Here, particles are serving as sacrificial mask for structuring. This approach has been particularly successful for structuring electrode materials, which can at the same time provide light harvesting functionality. These systems share many optical features with the colloidal assemblies discussed in the first part, but they as well give rise to novel plasmonic features. Such multifunctional electrodes can support propagating surface plasmon resoances, but as well may be used as ITO replacement due to their electric conductivity. The topography of such electrodes can reduce the reflectivity between media of different refractive index. Concomitantly, the increased surface area compared to flat analogs may lead to higher charge extraction, but calls for designed electrical properties.

The availability of countless synthesis methods yielding colloids with tailored optical properties as well as the manifold assembly strategies for monolayer preparation, providing control over inter-particle distance and assembly structure, represent a rich toolbox for light management in PV. In general, the light management structures can be integrated either into the PV medium or at the electrode interface very easily. In particular in the context of the world-wide increasing energy needs, the relevance of colloidal light management structures in PV will increase in the future. The progress in colloid synthesis has not only dramatically improved the control of particle properties, at the same time, up-scaling and consequently cost-reduction has been achieved for many particle types. Furthermore, colloidal assembly processes are in many cases, at least partially, based on self-assembly principles, allowing again for cost effective up-scaling to large areas.

In this review we highlighted that particularly a combination of tailor-made colloids with appropriate assembly methods opens pathways toward collective optical effects, which may lead to further enhancement concepts in PV. Other strategies such as panchromatic light management, which can be achieved by poly-disperse or non-spherical systems, or photoactive materials such as semi-conductor nanoparticles, have only briefly been addressed in this review. Yet, combining such systems with the outlined concepts may further contribute to clean energy generation.

## Acknowledgements

This study was funded by the European Research Council under grant ERC-2012-StG 306686 (METAMECH) as well as by the German Research Foundation (DFG) within the collaborative research center SFB 840.

## References

- [1] J. Albrecht, *Energ Policy* 35 (4) (2007) 2296.
- [2] A. Hagfeldt, et al. *Chem. Rev.* 110 (11) (2010) 6595.
- [3] S.D. Dimitrov, J.R. Durrant, *Chem. Mater.* 26 (1) (2014) 616.
- [4] J.H. Yum, et al. *Angew. Chem. Int. Ed.* 48 (49) (2009) 9277.
- [5] K. Driscoll, et al. *Nano Lett.* 10 (12) (2010) 4981.
- [6] J.H. Yum, et al. *Chem. Commun.* 44 (2007) 4680.
- [7] J. Bandara, et al. *Phys. Chem. Chem. Phys.* 13 (28) (2011) 12906.
- [8] H.W. Lin, et al. *Adv. Mater.* 24 (17) (2012) 2269.
- [9] S. Nishimura, et al. *J. Am. Chem. Soc.* 125 (20) (2003) 6306.
- [10] H.A. Atwater, A. Polman, *Nat. Mater.* 9 (3) (2010) 205.
- [11] F.X. Xie, et al. *Energy Environ. Sci.* 6 (11) (2013) 3372.
- [12] P. Reineck, et al. *Adv. Mater.* 24 (35) (2012) 4750.
- [13] Y. Tian, T. Tatsuma, *J. Am. Chem. Soc.* 127 (20) (2005) 7632.
- [14] Y. Takahashi, T. Tatsuma, *Appl. Phys. Lett.* 99 (2011) 182110.
- [15] B.I. MacDonald, et al. *Thin Solid Films* 558 (2014) 365.
- [16] H.K. Jun, et al. *Renew. Sustain. Energy Rev.* 22 (0) (2013) 148.
- [17] P.V. Kamat, *J. Phys. Chem. Lett.* 4 (6) (2013) 908.
- [18] C.-H.M. Chuang, et al. *Nat. Mater.* 13 (8) (2014) 796.
- [19] X. Lan, et al. *Nat. Mater.* 13 (3) (2014) 233.
- [20] A. Uddin, X.H. Yang, *J. Nanosci. Nanotechnol.* 14 (2) (2014) 1099.
- [21] M.L. Brongersma, et al. *Nat. Mater.* 13 (5) (2014) 451.
- [22] E. Stratakis, E. Kymakis, *Mater. Today* 16 (4) (2013) 133.
- [23] Q.Q. Gan, et al. *Adv. Mater.* 25 (17) (2013) 2385.
- [24] K.R. Catchpole, A. Polman, *Opt. Express* 16 (26) (2008) 21793.
- [25] J.R. Cole, N.J. Halas, *Appl. Phys. Lett.* 89 (15) (2006) 153120.
- [26] M.J. Mendes, et al. *Nanoscale* 6 (9) (2014) 4796.
- [27] D.H. Wang, et al. *Angew. Chem. Int. Ed.* 50 (24) (2011) 5519.
- [28] J. Yang, et al. *ACS Nano* 5 (8) (2011) 6210.
- [29] H. Choi, et al. *Nano Lett.* 13 (5) (2013) 2204.
- [30] S.W. Baek, et al. *Sci. Rep.* 3 (2013) 1726.
- [31] W.-F. Fu, et al. *Phys. Chem. Chem. Phys.* 15 (40) (2013) 17105.
- [32] M.K. Gangishetty, et al. *ACS Appl. Mater. Interfaces* 5 (21) (2013) 11044.
- [33] L.Y. Lu, et al. *Nano Lett.* 13 (1) (2013) 59.
- [34] B. Paci, et al. *Adv. Funct. Mater.* 21 (2011) 3573.
- [35] J.F. Qi, et al. *ACS Nano* 5 (9) (2011) 7108.
- [36] G.D. Spyropoulos, et al. *Appl. Phys. Lett.* 100 (2012) 213904.
- [37] S.W. Sheehan, et al. *J. Phys. Chem. C* 117 (2) (2013) 927.
- [38] S.D. Standridge, et al. *J. Am. Chem. Soc.* 131 (24) (2009) 8407.
- [39] S. Wooh, et al. *J. Mater. Chem. A* 1 (40) (2013) 12627.
- [40] Q. Xu, et al. *Opt. Express* 22 (5) (2014) A301.
- [41] J. Grandidier, et al. *Phys. Status Solidi A* 210 (2) (2013) 255.
- [42] F. Pastorelli, et al. *Adv. Opt. Mater.* 2 (2) (2014) 171.
- [43] M.D. Brown, et al. *Nano Lett.* 11 (2010) 438.
- [44] T. Kawakami, et al. *J. Phys. Chem. C* 117 (11) (2013) 5901.
- [45] W.J. Yoon, et al. *Sol. Energy Mater. Sol. Cells* 94 (2) (2010) 128.
- [46] D. Qu, et al. *Opt. Express* 19 (24) (2011) 24795.
- [47] J.F. Zhu, et al. *Appl. Phys. Lett.* 98 (15) (2011) 151110.
- [48] A. Polman, H.A. Atwater, *Nat. Mater.* 11 (3) (2012) 174.
- [49] K. Aydin, et al. *Nat. Commun.* 2 (2011) 517.
- [50] R.E. Bird, et al. *Sol. Energy* 30 (6) (1983) 563.
- [51] Y.S. He, et al. *J. Mater. Res.* 8 (12) (1993) 3131.
- [52] W.Z. Cai, et al. *Sol. Energy Mater. Sol. Cells* 94 (2) (2010) 114.
- [53] D. Muhlbacher, et al. *Adv. Mater.* 18 (22) (2006) 2931.
- [54] M. Rycenga, et al. *Chem. Rev.* 111 (6) (2011) 3669.
- [55] G. Mie, *Ann. Phys. (Berlin)* 25 (3) (1908) 377.
- [56] L.M. Liz-Marzán, *Photonik* 39 (2) (2007) 58.
- [57] C. Mätzler, et al., IET Electromagnetic Waves Series 52, Institution of Engineering and Technology, London, 2006.
- [58] C. Hanske, et al. *Nano Lett.* (2014), <http://dx.doi.org/10.1021/nl502776s> (accepted).
- [59] T.A.F. König, et al. *ACS Nano* 8 (6) (2014) 6182.
- [60] V. Myroshnychenko, et al. *Chem. Soc. Rev.* 37 (9) (2008) 1792.
- [61] M.B. Müller, et al. *ACS Nano* 8 (9) (2014) 9410.
- [62] K.A. Willets, R.P. Van Duyne, *Annu. Rev. Phys. Chem.* 58 (2007) 267.
- [63] P. Spinelli, A. Polman, *Opt. Express* 20 (S5) (2012) A641.
- [64] C. Hägglund, S.P. Apell, *J. Phys. Chem. Lett.* 3 (10) (2012) 1275.
- [65] B.J. Wiley, et al. *J. Phys. Chem. B* 110 (32) (2006) 15666.
- [66] R. Koidiyath, et al. *J. Mater. Chem. A* 1 (8) (2013) 2777.
- [67] S. Pillai, et al. *J. Appl. Phys.* 101 (9) (2007) 093105.
- [68] T.A. Erickson, J.W. Tunnell, Nanotechnologies for the Life Sciences, Wiley-VCH Verlag GmbH & Co. KGaA, 2007.
- [69] K.T. Yong, et al. *Colloids Surf. A* 290 (1–3) (2006) 89.
- [70] D. Paz-Soldan, et al. *Nano Lett.* 13 (4) (2013) 1502.
- [71] H. Warson, *Polym. Int.* 41 (3) (1996) 352.
- [72] H. Kawaguchi, *Prog. Polym. Sci.* 25 (8) (2000) 1171.
- [73] F.J. Schork, et al. in: M. Okubo (Ed.), Polymer Particles, vol. 175, Springer, Berlin/Heidelberg, 2005, p. 129.
- [74] K. Landfester, in: M. Antonietti (Ed.), Colloid Chemistry II, vol. 227, Springer, Berlin/Heidelberg, 2003, p. 75.
- [75] J.W. Goodwin, et al. *Colloid Polym. Sci.* 252 (6) (1974) 464.
- [76] M. Egen, R. Zentel, *Macromol. Chem. Phys.* 205 (11) (2004) 1479.
- [77] J. Grandidier, et al. *Adv. Mater.* 23 (10) (2011) 1272.
- [78] J.R. Nagel, M.A. Scarpulla, *Appl. Phys. Lett.* 102 (15) (2013) 151111.
- [79] W. Stober, et al. *J. Colloid Interface Sci.* 26 (1) (1968) 62.
- [80] C.J.S.G.W. Brinker, Sol-Gel Science: The Physics and Chemistry of Sol-Gel Processing, Academic Press, Inc., 1990.
- [81] M. Retsch, et al. *Nano Lett.* 11 (3) (2011) 1389.
- [82] J. Turkevich, et al. *Discuss. Faraday Soc.* 11 (1951) 55.
- [83] G. Frens, *Nat. Phys. Sci.* 241 (1973) 20.
- [84] J. Kimling, et al. *J. Phys. Chem. B* 110 (32) (2006) 15700.
- [85] C. Li, et al. *Nanoscale Res. Lett.* 6 (1) (2011) 440.
- [86] N.R. Jana, et al. *Langmuir* 17 (22) (2001) 6782.
- [87] N. Pazos-Perez, et al. *Langmuir* 28 (24) (2012) 8909.
- [88] J. Rodriguez-Fernandez, et al. *Langmuir* 22 (16) (2006) 7007.
- [89] J.Z. Niu, T.Z. Liu, *Nanotechnology* 18 (2007) 325607.
- [90] N.G. Bastus, et al. *Langmuir* 27 (17) (2011) 11098.
- [91] T. Konig, et al. *Plasmonics* 7 (3) (2012) 535.
- [92] H. Li, et al. *Langmuir* 29 (16) (2013) 5074.
- [93] H. Li, et al. *Langmuir* 30 (9) (2014) 2498.
- [94] D.D. Evanoff, G. Chumanov, *J. Phys. Chem. B* 108 (37) (2004) 13948.
- [95] D.D. Evanoff, G. Chumanov, *J. Phys. Chem. B* 108 (37) (2004) 13957.
- [96] N.G. Bastus, et al. *Chem. Mater.* 26 (9) (2014) 2836.
- [97] B. Nikoobakht, M.A. El-Sayed, *Chem. Mater.* 15 (10) (2003) 1957.
- [98] L. Scarabelli, et al. *ACS Nano* 8 (6) (2014) 5833.
- [99] A. Sanchez-Iglesias, et al. *Adv. Mater.* 18 (19) (2006) 2529.
- [100] P.S. Kumar, et al. *Nanotechnology* 19 (1) (2008) 015606.
- [101] W.X. Niu, et al. *J. Am. Chem. Soc.* 136 (8) (2014) 3010.
- [102] P. Mulvaney, *Langmuir* 12 (3) (1996) 788.
- [103] K.C. Ng, W.L. Cheng, *Nanotechnology* 23 (10) (2012) 105602.
- [104] M. Grzelczak, et al. *Chem. Soc. Rev.* 37 (9) (2008) 1783.
- [105] R. Sardar, et al. *Langmuir* 25 (24) (2009) 13840.
- [106] T.K. Sau, A.L. Rogach, *Adv. Mater.* 22 (16) (2010) 1781.
- [107] S.J. Tan, et al. *Nat. Nanotechnol.* 6 (5) (2011) 268.
- [108] G.S. He, et al. *J. Appl. Phys.* 105 (2) (2009) 023110.
- [109] L.M. Liz-Marzán, et al. *Langmuir* 12 (18) (1996) 4329.
- [110] T. Ung, et al. *J. Phys. Chem. B* 105 (17) (2001) 3441.
- [111] I. Pastoriza-Santos, et al. *Chem. Mater.* 18 (10) (2006) 2465.
- [112] S. Wu, et al. *Colloid Polym. Sci.* 291 (3) (2013) 585.
- [113] N.M. Bahadur, et al. *J. Colloid Interface Sci.* 355 (2) (2011) 312.
- [114] M. Giersig, P. Mulvaney, *Langmuir* 9 (12) (1993) 3408.
- [115] J. Fink, et al. *Chem. Mater.* 10 (3) (1998) 922.
- [116] T.P. Bigioni, et al. *Nat. Mater.* 5 (4) (2006) 265.
- [117] M. Karg, et al. *Chem. Eur. J.* 17 (16) (2011) 4648.
- [118] K.S. Mayya, F. Caruso, *Langmuir* 19 (17) (2003) 6987.
- [119] S.J. Barrow, et al. *Nano Lett.* 11 (10) (2011) 4180.
- [120] S.J. Barrow, et al. *Nat. Commun.* 3 (2012) 1275.
- [121] C.H. Lalander, et al. *ACS Nano* 4 (10) (2010) 6153.
- [122] H. Yao, et al. *Nanotechnology* 18 (1) (2007) 015102.
- [123] T. Thai, et al. *Angew. Chem. Int. Ed.* 51 (35) (2012) 8732.
- [124] S. Ehler, et al. *ACS Nano* 8 (6) (2014) 6114.
- [125] W.L. Cheng, et al. *Nat. Mater.* 8 (6) (2009) 519.
- [126] B. Ebeling, P. Vana, *Macromolecules* 46 (12) (2013) 4862.
- [127] M. Karg, et al. *ChemPhysChem* 7 (11) (2006) 2298.
- [128] M. Karg, et al. *Colloid Polym. Sci.* 289 (5–6) (2011) 699.
- [129] R. Contreras-Caceres, et al. *Adv. Mater.* 20 (9) (2008) 1666.
- [130] M. Karg, et al. *Langmuir* 27 (2) (2011) 820.

- [131] M. Muller, et al. *Nanoscale* 4 (7) (2012) 2491.
- [132] K.C. Grabar, et al. *Anal. Chem.* 67 (4) (1995) 735.
- [133] C.D. Keating, et al. *J. Chem. Educ.* 76 (7) (1999) 949.
- [134] S. Jaber, et al. *Phys. Chem. Chem. Phys.* 13 (13) (2011) 5576.
- [135] R.M. Bright, et al. *Langmuir* 14 (20) (1998) 5695.
- [136] M.K. Gupta, et al. *Small* 9 (17) (2013) 2979.
- [137] T. Konig, et al. *Part. Part. Syst. Char.* 31 (2) (2014) 274.
- [138] P.K. Jain, et al. *Nano Lett.* 7 (7) (2007) 2080.
- [139] F.J. Beck, et al. *J. Appl. Phys.* 105 (11) (2009) 114310.
- [140] B.J. Soller, et al. *Opt. Lett.* 26 (18) (2001) 1421.
- [141] C. Battaglia, et al. *ACS Nano* 6 (3) (2012) 2790.
- [142] Z.F. Yu, et al. *Proc. Natl. Acad. Sci. U. S. A.* 107 (41) (2010) 17491.
- [143] T. Konig, et al. *ACS Appl. Mater. Interfaces* 5 (13) (2013) 6009.
- [144] C.X. Lin, M.L. Povinelli, *Opt. Express* 17 (22) (2009) 19371.
- [145] Y.C. Lee, et al. *Opt. Express* 16 (11) (2008) 7969.
- [146] Z.F. Yu, et al. *Opt. Express* 18 (19) (2010) A366.
- [147] S.E. Han, G. Chen, *Nano Lett.* 10 (3) (2010) 1012.
- [148] D. Pacifici, et al. *Phys. Rev. B* 77 (11) (2008) 115411.
- [149] A. Baba, et al. *ACS Appl. Mater. Interfaces* 3 (6) (2011) 2080.
- [150] Y. Yao, et al. *Nat. Commun.* 3 (2012) 664.
- [151] A. Moreau, et al. *Nature* 492 (7427) (2012) 86.
- [152] J.B. Lassiter, et al. *Nano Lett.* 13 (12) (2013) 5866.
- [153] T. Kraus, et al. *Adv. Funct. Mater.* 23 (36) (2013) 4529.
- [154] Y.H. Zheng, et al. *Adv. Funct. Mater.* 23 (12) (2013) 1519.
- [155] N. Pazos-Perez, et al. *Angew. Chem. Int. Ed.* 51 (51) (2012) 12688.
- [156] X. Chen, et al. *Nano Lett.* 12 (5) (2012) 2187.
- [157] C.H. Lu, et al. *Soft Matter* 3 (12) (2007) 1530.
- [158] A. Schweikart, A. Fery, *Microchim. Acta* 165 (3–4) (2009) 249.
- [159] M. Pretzl, et al. *Langmuir* 24 (22) (2008) 12748.
- [160] M. Retsch, et al. *Soft Matter* 6 (11) (2010) 2403.
- [161] C. Farcau, et al. *Appl. Phys. B: Lasers Opt.* 106 (4) (2012) 849.
- [162] M. Born, E. Wolf, *Principles of Optics Electromagnetic Theory of Propagation, Interference and Diffraction of Light*, 7th (expanded) ed., Cambridge Univ. Press, Cambridge, 2002, XXXIII pp..
- [163] S.-M. Yang, et al. *Small* 2 (4) (2006) 458.
- [164] C.L. Haynes, R.P. van Duyne, *J. Phys. Chem. B* 105 (2001) 5599.
- [165] X.H. Li, et al. *J. Appl. Phys.* 114 (4) (2013) 044301.
- [166] H.Y. Wei, et al. *Energy Environ. Sci.* 6 (4) (2013) 1192.
- [167] J.P. Mailoa, et al. *J. Phys. D: Appl. Phys.* 47 (8) (2014) 085105.
- [168] M.M. Adachi, et al. *Sci. Rep.* 3 (2013) 2928.
- [169] J. Zhu, et al. *Appl. Phys. Lett.* 100 (2012) 143109.
- [170] N. Vogel, et al. *Macromol. Chem. Phys.* 212 (2011) 1719.
- [171] N. Vogel, et al. *Nat. Commun.* 4 (2013) 2176.
- [172] B. Wu, et al. *J. Phys. Chem. C* 116 (28) (2012) 14820.
- [173] A. Kirkeminde, et al. *Nanoscale* 4 (15) (2012) 4421.
- [174] N.N. Lal, et al. *Opt. Express* 19 (2011) 11256.
- [175] N.N. Lal, et al. *Phys. Rev. B* 85 (24) (2012) 245318.
- [176] S. Xie, et al. *Opt. Mater. Express* 4 (2) (2014) 321.
- [177] J. Zhu, et al. *Nano Lett.* 9 (1) (2009) 279.
- [178] J. Zhu, et al. *Nano Lett.* 10 (6) (2010) 1979.
- [179] C. Genet, T.W. Ebbesen, *Nature* 445 (7123) (2007) 39.
- [180] F.J. Garcia-Vidal, et al. *Rev. Mod. Phys.* 82 (1) (2010) 729.
- [181] T.H. Reilly, et al. *Nano Lett.* 4 (2010) 615.
- [182] T.H. Reilly, et al. *Appl. Phys. Lett.* 92 (24) (2008) 243304.
- [183] E. Metin Akinoglu, et al. *Appl. Phys. Lett.* 103 (17) (2013) 171106.
- [184] A.J. Morfa, et al. *J. Appl. Phys.* 114 (5) (2013) 054502.
- [185] W.A. Luhman, et al. *Appl. Phys. Lett.* 99 (10) (2011) 103306.
- [186] S.Y. Chou, W. Ding, *Opt. Express* 21 (1) (2013) A60.
- [187] T.G. Chen, et al. *Prog. Photovolt.* 22 (4) (2014) 452.
- [188] X. Deng, et al. *Adv. Mater.* 23 (2011) 2962.
- [189] J.W. Menezes, et al. *Adv. Funct. Mater.* 20 (2010) 3918.
- [190] Y.-S. Hsiao, et al. *J. Phys. Chem. C* 115 (23) (2011) 11864.